UNIVERSITY OF CALIFORNIA
RIVERSIDE

# Two-Dimensional Van der Waals Materials for Thin Film Transistor Applications

A Dissertation submitted in partial satisfaction
of the requirements for the degree of

Doctor of Philosophy

in

Materials Science and Engineering

by

Aaron Scott George

December 2014

Dissertation Committee:

Dr. Cengiz S. Ozkan, Co-Chairperson
Dr. Mihrimah Ozkan, Co-Chairperson
Dr. Elaine Haberer
Dr. Sandeep Kumar

The Dissertation of Aaron Scott George is approved:

_____

_____

_____

Committee Co-Chairperson

_____

Committee Co-Chairperson

University of California, Riverside

**Acknowledgements**

I would like to express gratitude to all of my friends and colleagues who supported me during my Ph.D. work. Much of the work of chapter 4 of this dissertation was previously published in Advanced Functional Materials (DOI:10.1002/adfm.201402519).

First, I would like to thank my research advisors Dr. Cengiz S. Okzan and Dr. Mihrimah Ozkan for their financial support throughout the course of my Ph.D. work. I have appreciated the freedom to pursue research and generate my own ideas for projects that interested me the most. I believe that their encouragement of independent ideas and work has enhanced my research learning experience.

I would also like to thank the members of my qualifying and Ph.D. defense: Dr. Elaine Haberer, Dr. Masaru Rao, Dr. Kumar Sandeep, my advisor Dr. Cengiz Ozkan, and my co-advisor Dr. Mihrimah Ozkan.

I would like to thank the staff of the UCR CNSE cleanroom facility: Mark Heiden, Dexter Humphrey, and Dong Yan. Every one of the cleanroom facility staff has worked around the clock to provide the best services possible in the CNSE facility. Thank you for dealing with the daily problems and frustrations of supporting the research of all of the university graduate students. I have also appreciated the effort made to

ensure the upkeep of fabrication equipment by the CNSE staff and the guidance I have received which helped me to learn far more than I could have otherwise.

Finally, I would like to give my thanks to my family for always supporting me and believing in me. I would especially like to thank my wife for her understanding and supporting me at all times.

ABSTRACT OF THE DISSERTATION

Two-Dimensional Van der Waals Materials for Thin Film Transistor Applications

by

Aaron Scott George

Doctor of Philosophy, Graduate Program in Materials Science and Engineering
University of California, Riverside, December 2014
Dr. Cengiz S. Ozkan, Co-Chairperson
Dr. Mihrimah Ozkan, Co-Chairperson

Research on two-dimensional nanomaterials has become a topic of considerable interest since the pioneering work experimentally introducing the two-dimensional carbon allotrope of graphene in 2004. The atomically thin hexagonally arranged carbon crystal structure has offered the opportunity for numerous studies in condensed matter physics and materials science, revealing new phenomenon and remarkable properties. Graphene has excellent chemical and mechanical stability, allowing researchers to probe the properties of graphene in a wide variety of applications and in contact with a wide variety of materials. Ballistic transport of graphene at room temperature suggests that graphene would be poised to enter in to a wide variety of microelectronic application;

however, synthesis methods and surface effects have so far limited the widespread use of graphene. Additionally, the absence of electronic band gap in graphene, classifying it as a "semi-metal", limits the use of graphene to areas other than logic applications.

In this work, fabrication methods for the improved synthesis graphene and selected two-dimensional transition metal dichalcogenides, molybdenum disulfide and tungsten disulfide, are presented for thin film transistor applications. First, the introduction of thin film zwitterionic polymer interlayers in graphene devices is outlined as a means to reduce the contact resistance between metal contacts and the underlying graphene layer. Second, a self-assembly nanoscale lithography process utilizing diblock copolymer templates as an etching mask directly on the surface of graphene is shown as a method to introduce a band gap in graphene due to quantum confinement effects. The third chapter applies to another class of two-dimensional materials, transition metal dichalcogenides, which, unlike graphene, can exhibit suitable electronic band structures for logic applications. When the thickness of these transition metal dichalcogenides is reduced to a single atomic layer, electronic band states transition from an indirect band gap to a direct band gap. A wafer-scale method for the synthesis of atomically thin transition metal dichalcogenides by the thermolysis of spin coated precursors is introduced which holds promise for next-generation low-power consumption applications.

## Table of Contents

## List of Figures

# Chapter 1 - Introduction

## 1.1 - The History of Graphene

Graphene, a single atomic carbon layer in a hexagonal lattice structure, has been shown to have exceptional properties such as high mobility[1], ballistic transport[2], high thermal conductivity[3], high optical transmittance[4] and excellent mechanical hardness[5]. In 1947, P.R. Wallace firstly theoretically explored the concept of graphene and pointed out that graphene would exist as a zero band gap semiconductor[6]. In 1984, Mele, E.J. et. al. pointed out the emergent massless Dirac equation to describe the electrons around the Fermi level[7]. The term "graphene" was first coined by Mouras et. al. in 1987 to refer to the single sheet of graphite within the graphite intercalation compounds[8]. Prior to the separation of graphene in 2004[9], it was argued that monolayer graphene could not exist because it would be thermodynamically unstable and an atomic monolayer would roll or fold. Later research revealed intrinsic ripples in atomic layer graphene, which are believed to suppress thermal fluctuation in graphene and prevent graphene from rolling or folding[10]. The discovery of graphene was accredited to Novoselov et al., when the extraction and characterization of single atomic layer thick crystallites from highly ordered pyrolytic graphite was achieved mechanical exfoliation using 'Scotch tape'. Since then, significant scientific advances have been made in analyzing the spectacular properties and interesting interactions of atomically thin materials.

## 1.2 - Structure and Properties of Graphene

Materials properties are influenced incredibly not only by chemical composition but also by physical structure, or morphology. Carbon is capable of taking many different allotropes due to its valency. Two of the most well-known carbon allotropes, diamond and graphite have strikingly different properties. For instance, diamond is intrinsically an electrical insulator known for dispersing light and for being the hardest natural mineral. Hence, diamond has found applications in jewelry and industrial applications. In contrast, graphite is electrically conductive in plane and has thus found applications such as in arc lamps. Weak van der Waals bonding within the planes of graphite has also allowed the use of graphite as a lubricant in common applications.

At the nanoscale, carbon allotropes feature a rich variation of morphologies and properties. Most notably, buckminsterfullerene, carbon nanotubes, and graphene have drawn significant interest in the scientific community. Buckminsterfullerene was discovered first in 1980s, and in 1996, the Nobel Prize was awarded jointly to Robert F. Curl Jr., Sir Harold W. Kroto and Richard E. Smalley "for their discovery of fullerenes" [11]. Buckminsterfullerene, or buckyball, is a spherical fullerene molecule with the formula $C_{60}$. Accreditation of the discovery of carbon nanotubes is a debated matter[12], but the prediction of high conductivity single-walled carbon nanotubes[13] and the synthesis of multi-walled carbon nanotubes in the early 1990s sparked a huge interest in carbon nanotubes. Carbon nanotubes are a carbon allotrope with a cylindrical nanostructure and unprecedented length-to-diameter ratio of up to 132,000,000:1[14]. Semiconducting or

metallic electrical properties of carbon nanotubes are determined by the chirality of the carbon atoms[15–17]. Graphene takes the form of a single layer of six-membered carbon rings extending laterally. Although discovered later than all of the previously described carbon allotropes, graphene has been described as the "mother of all graphitic forms" due the simple visualization of the formation of other carbon allotropes by the wrapping, rolling, or stacking of graphene.

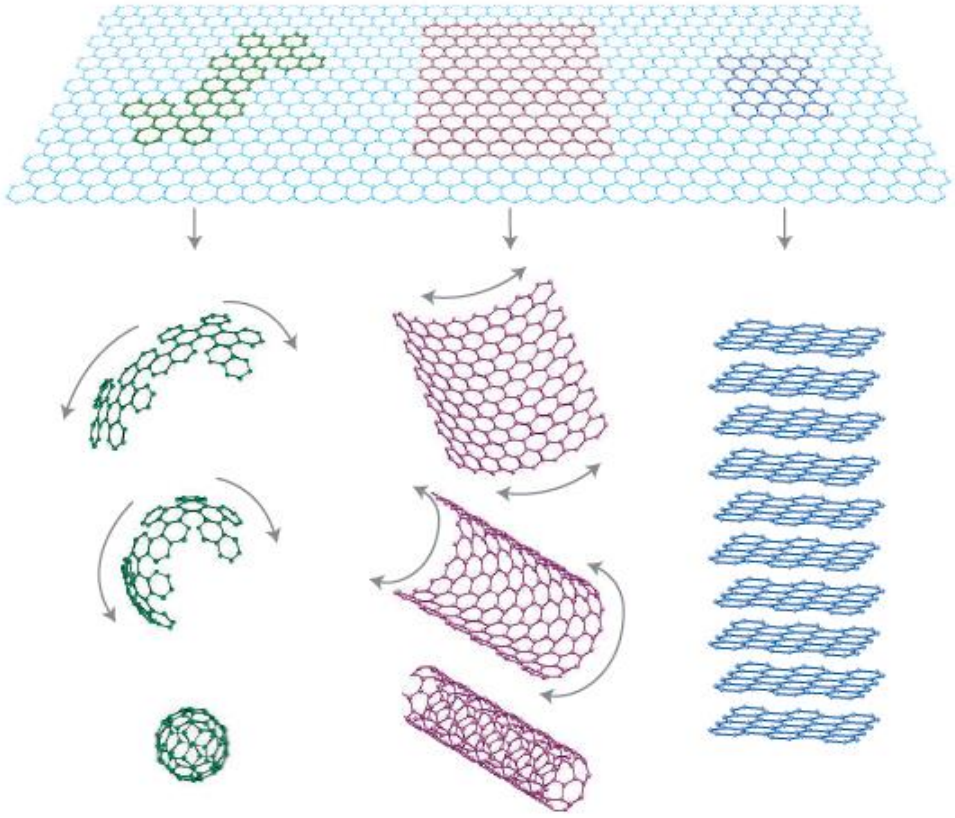

**Figure 1.** Mother of all graphitic forms. Graphene is a 2D building material for carbon materials of all other dimensionalities. It can be wrapped up into 0D buckyballs, rolled into 1D nanotubes or stacked into 3D graphite[1].

Andre Geim and Konstantin Novoselov were awarded the Nobel Prize in Physics "for groundbreaking experiments regarding the two-dimensional material graphene"[18]. Graphene structure is that of a single-layer of carbon atoms bound together in a two-dimensional $sp^2$ bonding arrangement. The band structure of graphene can be calculated using nearest-neighbor tight-binding model approximations, based on the $2p_z$ orbitals. Considering hopping only occurs between nearest neighbor atomic sites, the low-level energy bands of the π electrons can be described by the Dirac-like Hamiltonian:

$$H_{k'} = \begin{pmatrix} 0 & k_x - ik_y \\ k_x - ik_y & 0 \end{pmatrix} \quad (1)$$

$$H_{k'} = \begin{pmatrix} 0 & k_x + ik_y \\ k_x - ik_y & 0 \end{pmatrix} \quad (2)$$

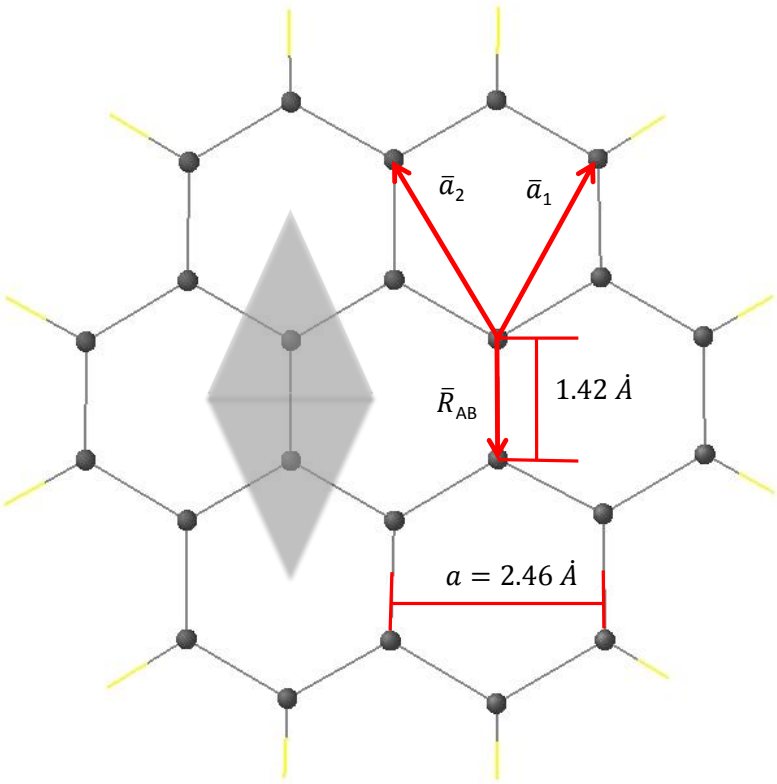


**Figure 2.** Graphene lattice. Grey-shaded area indicates the primitive unit cell. The hexagonal bond length is $d_{cc}$ =1.42 angstroms and the lattice constant is 2.46 angstroms.

In forming the layers of graphite, graphene layers stack in an ABA Bernal stacking form, where each layer shows a thickness of 0.34 nm. Electronic behavior is influenced by the stacking of carbon layers. In the case of bilayer graphene, four atoms exist in a unit cell, labeled $A_1$, $B_1$, $A_2$ and $B_2$ (Figure 2), where each subscript numerical index represents the different layers[19]. Considering nearest neighbor hoping in-plane and out of plane, Hamiltonians for these bands can be expressed as[20]:

$$H_k = \frac{\hbar^2}{2m}\begin{pmatrix} 0 & (k_x - ik_y)^2 \\ (k_x + ik_y)^2 & 0 \end{pmatrix} \quad (3)$$

$$H_k = \frac{\hbar^2}{2m}\begin{pmatrix} 0 & (k_x - ik_y)^2 \\ (k_x - ik_y)^2 & 0 \end{pmatrix} \quad (4)$$

The band structures of single-layer and bilayer graphene are shown in Figure 3. In the case of single-layer graphene, the electronic band structure is linearly dispersive around K and K' and shows zero band gap. Low-energy carriers in graphene are massless around the point of charge neutrality and exhibit relativistic speeds[21]. This fascinating electronic band structure is the reason for observations of ambipolar electric field effect and ballistic properties presenting extremely high mobilities. On the other hand, the electronic band structure of bilayer graphene presents two groups of parabolic bands by interlayer coupling and the properties of single-layer graphene are not preserved.

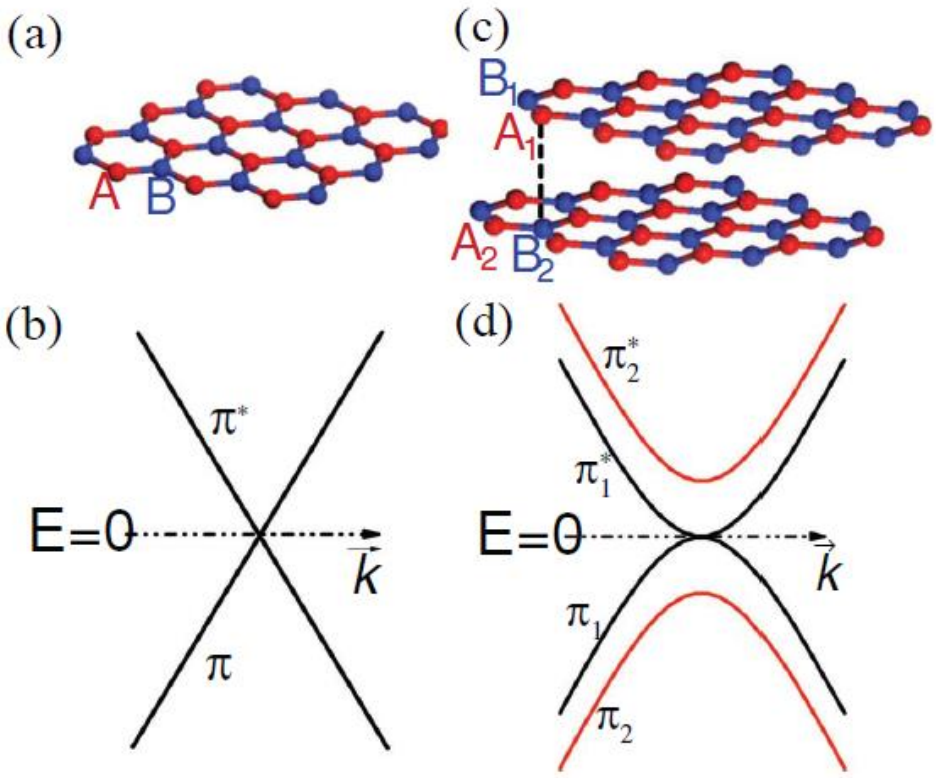


**Figure 3.** Crystal structures of (a) graphene single layer and (c) AB-stacked bilayer. The unit cell of single layer graphene and bilayer graphene consist of 2 and 4 atoms in each unit cell, respectively. (b) The hopping between nearest neighbor atom sites A and B resulting the linear dispersive electronic band structure. (d) The interlayer coupling for bilayer graphene cannot be ignored as the hopping between $A_1$ and $B_2$ affected the electronic band structure and resulting two parabolic electronic bands[19].

## 1.3 - Synthesis of Graphene

Since the 1970s, researchers have been using a variety of different methods to achieve very thin films of graphite like epitaxial growth[22], chemical exfoliation[23] and mechanical exfoliation[24]. However, between this period and 2004, the unique properties and potential applications of graphene had not been extensively explored and graphene did not attract the amount of attention as it has since 2004[25]. A key difference between the approach of Geim's group and predecessors is in characterization method. The major approach of Geim's group was to transfer graphitic layers on to silicon substrates with 300 nm oxide thickness, providing high optical contrast, which allows researchers to efficiently identify the number of graphene layers by optical microscopy. This approach proved to be reliable and easy, thus attracted immediate attention for further fundamental research[26,27]. Since then, various approaches including mechanical exfoliation, chemical exfoliation, epitaxial growth from SiC, and chemical vapor deposition (CVD) have been employed to produce graphene. Each of these methods has varying degrees of quality and cost of production. These main synthesis routes are categorized in the following sections.

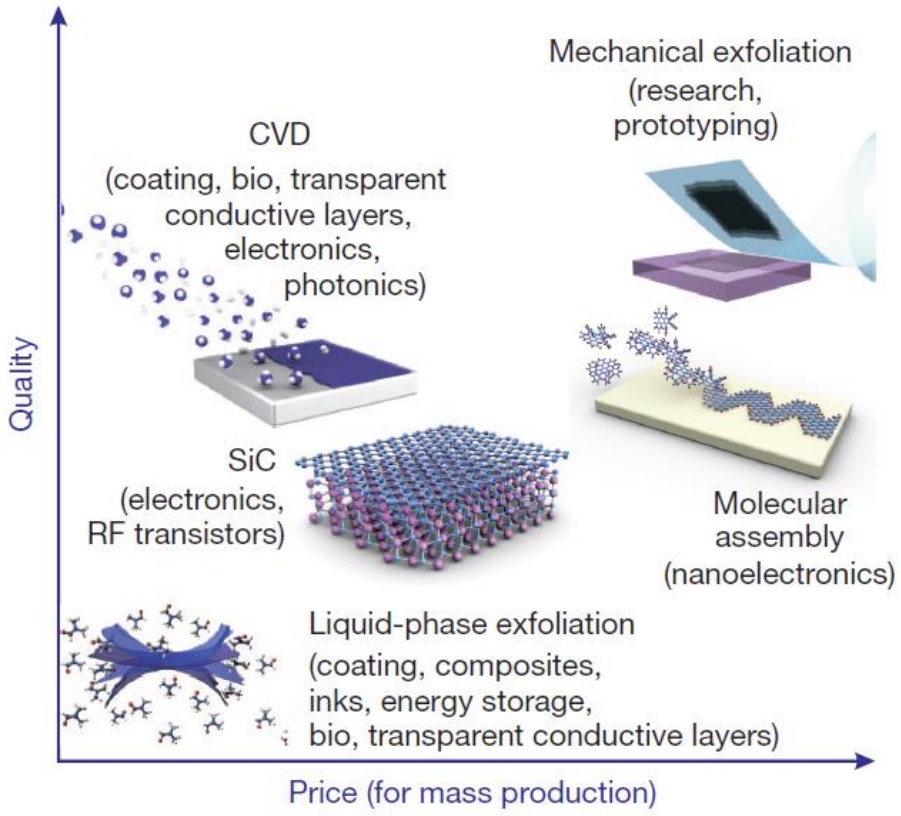


**Figure 4.** There are several methods of mass-production of graphene, which allow a wide choice in terms of size, quality and price for any particular application[28].

### 1.3.1 - Exfoliation and Cleavage

Weak Van der Waals forces between the layers of graphite allow single layer graphene to be exfoliated or cleaved by mechanical or chemical energy. As of 2014, mechanical exfoliation has produced graphene with the highest electron mobility and the lowest number of defects[29]. The most popular method requires multiple exfoliation steps,

where each cleaved slice contains fewer and fewer graphitic layers until only one atomic layer remains. A small graphene flake is shown in Figure 5.

Among important characterizations methods of graphene, Raman spectroscopy is one of the most commonly used techniques. Raman spectroscopy is a characterization method based on the inelastic scattering of light by matter. Due to the optical nature of Raman spectroscopy, the method is essentially nondestructive and noninvasive. Raman spectroscopy techniques are widely available, relatively simple to perform, and possible to carry out at room temperature under ambient temperature. Instrument setup involves the focusing of infrared or visible light through a frequently available laboratory microscope. Furthermore, Raman spectroscopy is highly sensitive to the physical and chemical properties of materials. For these reasons, Raman spectroscopy has become one of the most important tools for nanoscience and nanotechnology[30].

Raman spectroscopy has been established by experimental research as well as theory based on optics, solid state physics and chemistry. Changes in the environment that have been investigated as experimental parameters for Raman spectroscopy include light polarization[31], photon energy[32], temperature[26], and pressure[33]. Raman spectroscopy has been extremely successful in advancing the understanding of graphene[34,35]. Graphene has become one of the most commonly studied materials to be studied by Raman spectroscopy due to the interesting solid state physics of graphene and impact of graphene on nanoscience and nanotechnology.

Exfoliated graphene has allowed for fundamental studies in Raman spectroscopy. In graphene, two of the main peaks of interest are the G-peak (~1580 $cm^{-1}$) and the 2D peak (2680 $cm^{-1}$). The G/2D peak ratio can be used as an indicator of the number of layers in exfoliated graphene samples[36]. Raman spectroscopy indicated that the edges of the imaged flake are around two atomic layers. The narrow linewidth of peaks is characteristic of exfoliated graphene.

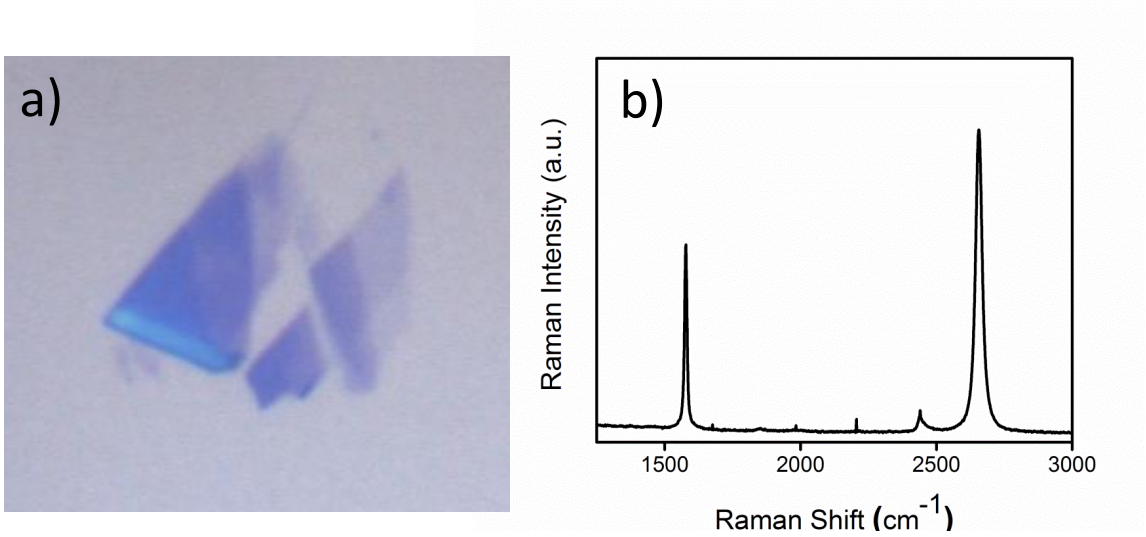


**Figure 5. (**a) Optical image and (b) Raman spectroscopy of exfoliated graphene.

Another synthesis approach to graphene is commonly called reduced graphene oxide. In this approach partially reduced graphene oxide (GO) nanosheets are produced by ultra-sonication of the graphite oxide flakes in aqueous suspension. Reduction of graphene oxide nanosheets by hydrazine hydrate or annealing in $Ar/H_2$ environment has been shown to produce monolayer graphene sheets[37,38]. However, these methods have

been shown to have insufficient removal of functional groups. Furthermore, over-oxidation has been shown to produce permanent defects in resultant graphene layers. To overcome the drawbacks of the reduced graphene oxide treatment, liquid exfoliation in organic solvent N-methylpyrrolidone (NMP) without oxidization of graphite was proposed by Hernandez et al. in 2008[39]. This process showed the promise of large scale production of graphene layers with high quality. Unfortunately, nothing prevents the graphene sheets from restacking, due to van der Waals forces[40]. The concentration of graphene in NMP was limited to 2.1 mg/mL. The maximum concentration of graphene in solution, without any prior chemical treatment, was increased to 5.33 mg/mL using 1-hexyl-3-methylimidazolium hexafluorophosphate as the dispersing liquid medium[41].

The major limitation for the synthesis of graphene by exfoliation is the inability to produce a high yield of single layer graphene with little to no defects. Graphene flakes produced by exfoliation methods are generally on the micrometer-scale, limiting electronics applications of graphene using exfoliation methods. Therefore, other methods have been developed to increase the area of continuous single atomic layer graphene.

### 1.3.2 - Epitaxial Growth of Graphene on Silicon Carbide

Epitaxial growth of graphene on SiC remains a promising synthesis technique. Epitaxy refers to the deposition of a crystalline overlayer on an underlying crystalline substrate. In the case of an epitaxial graphene layer on SiC, van der Waals forces are weak enough to preserve the electronic band structure of two-dimensional graphene, even

in few-layer graphene[42,43]. While the electronic properties of some multi-layer epitaxial graphene layers are identical to that of a single layer[44], other cases demonstrate that the electronic properties can be affected and show properties similar to that of bulk graphite[45]. These effects have been explained theoretically and they are related to the symmetry of the interlayer interactions. Many of the exciting electronic properties of graphene have been realized using epitaxial graphene layers on SiC. For example, the Dirac cone electronic band structure was first visualized in this material[46,47] and graphene on SiC exhibits massless Dirac fermions, even without transfer[48–52]. Furthermore, charge carrier mobilities of epitaxial graphene are similar to that of mechanically exfoliated graphene on $SiO_2$[53].

Epitaxial graphene on SiC can be patterned using standard microelectronics methods. Synthesis of epitaxial graphene on SiC allows for direct electrical characterization due to synthesis on semi-insulating substrate[54]. Original experiments on graphite formation on 6H-SiC(0001) and $(000\bar{1})$ surfaces were performed by van Bommel et al[55]. They showed that epitaxial graphite can be produced by heating SiC substrates at temperatures between 1000°C and 1500°C in ultrahigh vacuum ($10^{-6}$ Torr), sublimating Si to yield a carbon rich surface. More recently, researchers have synthesized epitaxial graphene at lower temperatures[56] and at atmospheric pressure[57], significant developments towards producing cost-effective, wafer-scale graphene. The area of epitaxial graphene layers is limited only by the size of the SiC substrate. Utilizing differences in growth mechanism between Si- and C-terminated surfaces, graphene can be grown in a wide variety of forms. Homogeneous monolayer, bilayer, and trilayer

graphene can be synthesized on SiC; as well as twisted bilayer graphene and anisotropic graphene, due to steps on the SiC. A significant potential application of epitaxial graphene is in high-frequency transistors, the IBM group has shown radio-frequency graphene field-effect transistor (FET) had the highest measured cutoff with up to 300 GHz cutoff frequency[58]. However, due to the high substrate cost and typically high-temperature, epitaxial graphene on SiC will likely be limited to high-value applications.

### 1.3.3 - Chemical Vapor Deposition

Chemical vapor deposition (CVD) shows promise as the future graphene synthesis technique graphene because it can produce large-area, layer-controlled, graphene at a lower-cost than epitaxial growth methods. Reports of the synthesis of few-layer graphene by CVD date back to 1975[22]. However, extensive research on thin graphitic carbon films by CVD began after the properties of graphene were revealed in 2004. In 2006, Somani et al. grew graphene layers using nickel metal catalyst substrates, revealing a favorable new method for graphene synthesis[59]. Nevertheless, intense research has been performed since this time in order to improve control over thickness, uniformity, and properties of CVD-synthesized graphene.

CVD synthesis method involves the introduction of carbon to metal catalyst substrates by thermally cracking hydrocarbon gas sources. Typically, gas flows are controlled to create an environment of three gases, one inert carrier gas, hydrogen, and one hydrocarbon gas. Choice of metal catalyst substrate affects the nature of the growth

mechanism of graphene due to different carbon solubility properties. Differences between the two most common graphene catalysts, nickel and copper, are discussed in this section.

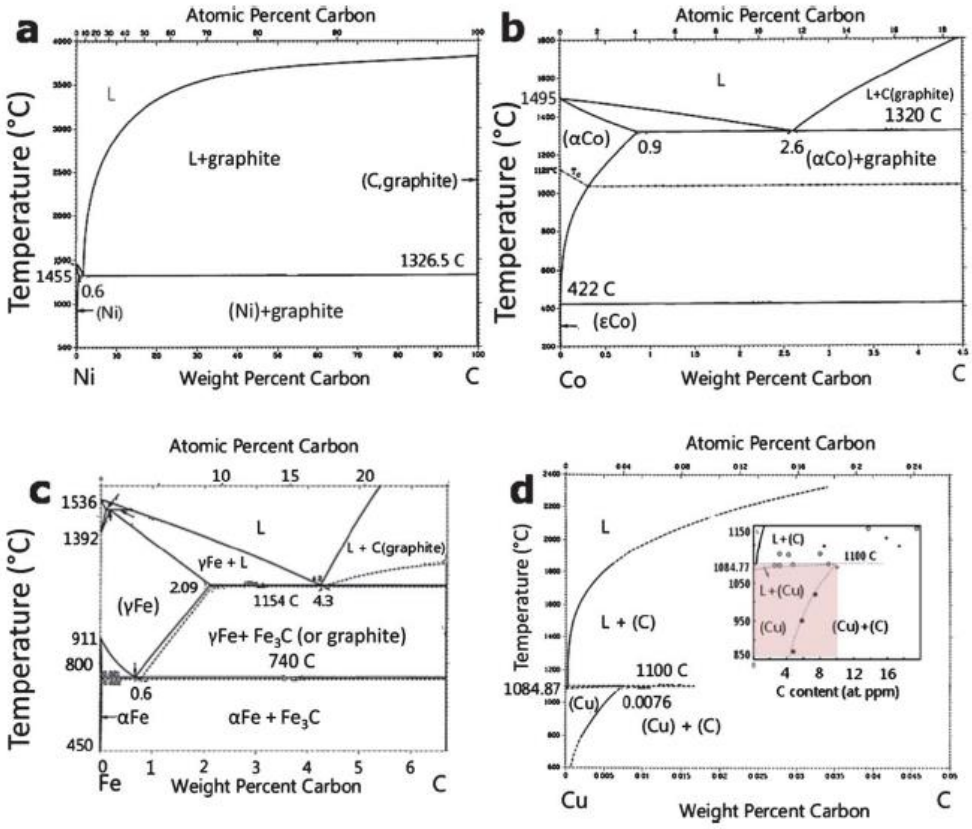


**Figure 6.** Binary phase diagrams of transition metals and carbon: (a) Ni–C; (b) Co–C; (c) Fe–C; (d) Cu–C. The low carbon solubility in Cu, of 0.008 weight % at 1084°C as reported is highlighted in the inset of panel (d) for the temperature and composition of interest for graphene growth[60].

For nickel catalyst substrates, the synthesis of graphitic carbon occurs by the diffusion of carbon into nickel and, upon cooling, out-diffusion and precipitation of

graphitic layers on the nickel surface. Due to the diffusion-precipitation mechanism of graphene growth using nickel catalyst substrates, difficulties arise concerning the thickness and uniformity of resulting graphene layers. Few-nm thick (1-2 nm) graphene films were grown on nickel foil, as early as 2007 through CVD synthesis[61,62]. Thin polycrystalline nickel films (<500 nm) have also been utilized as a method to control the thickness of graphene films[63,64]. In 2012, it was shown using nickel thin films that after eliminating supply of methane source gas, hydrogen exposure can lead to improved uniformity of resulting few-layer graphene layers on nickel[65].

Growth on polycrystalline nickel thin films (300-500 nm) was carried out at a growth temperature of 1000°C under methane source gas at 700 Torr. In the first step of the procedure, the furnace was ramped up to 1000°C from room temperature over a 25 minute period under a flow of 500 sccm Ar and 200 sccm $H_2$. The temperature was allowed to stabilize at 1000°C for 2 minutes before introducing 30 sccm $CH_4$ as the carbon source gas. Methane was allowed to flow for 3-5 minutes, after which the flow was turned off and the chamber was allowed to cool to room temperature.

Even on nickel thin films, decreasing the number of graphene layers to one single layer was unobtainable. Furthermore, the size and thickness of graphene domains was observed to be irregular by optical microscopy as shown in Figure 7. The properties of the synthesized carbon layers were characterized by Raman spectroscopy directly on the nickel surface. The weak Raman spectroscopy of carbon layers obtained by CVD growth on nickel thin films indicated the presence of multilayer graphene or graphite. A high

G/2D peak ratio and the asymmetrical shape of the 2D peak signified the presence of multilayer graphene[34,66].

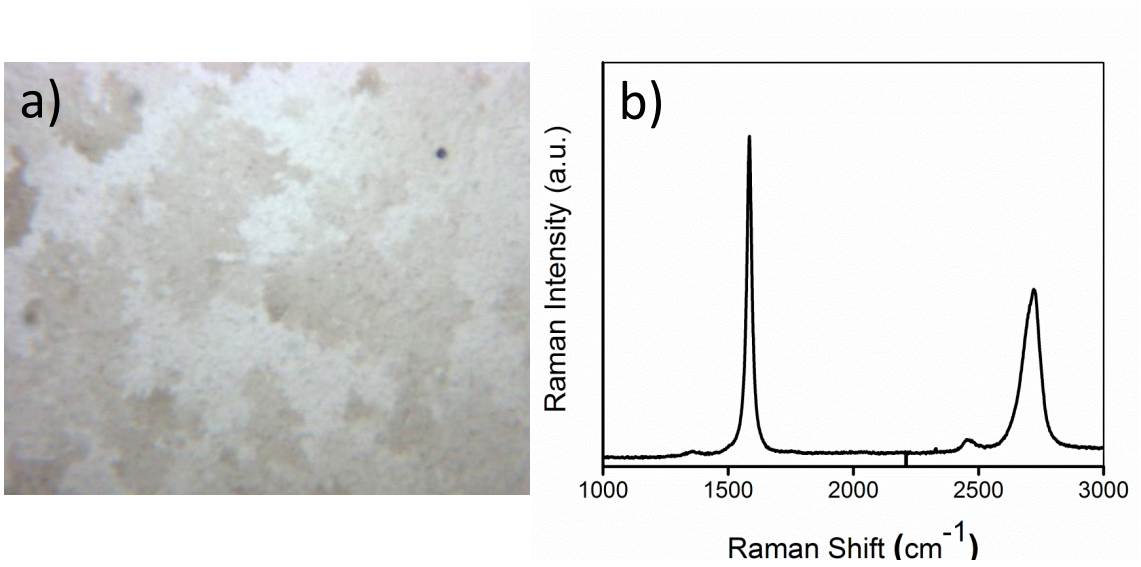


**Figure 7. (**a) Optical image and (b) Raman spectroscopy of graphene prepared by CVD synthesis on the surface of nickel.

Copper metal catalyst substrates have very low carbon solubility[67]. On copper, growth occurs through a surface catalyzed process. In copper catalyzed synthesis, hydrogen is first absorbed on to the surface of the copper catalyst substrate, which chemically provides sites for the absorption of hydrocarbon species to the copper layer. Surface absorbed hydrocarbon species are activated by hydrogen and the absorption of additional hydrocarbon species becomes thermodynamically favorable, forming multimeric species on the surface. A graphitic layer expands from the initial surface absorbed hydrocarbon seed forming a graphene grain, which expands as a function of

growth time on the copper surface. This copper catalyzed graphene growth, has become the most common CVD graphene synthesis method due to the ability to form large-area graphene films which compose of, almost exclusively, single-layer.

Single-layer graphene was grown on copper foil catalyst by Ruoff's group[68]. Following the discovery of copper catalyzed growth, process improvements towards high-quality, large-area graphene have progressed rapidly. Recently, ballistic transport was observed in graphene synthesized by the copper catalyst CVD method[69]. Scattering effects at graphene grain junctions have prompted research towards increasing the size of graphene grains. Recently, graphene grains with diameters in the mm-range were achieved by using oxygen as a means to decrease the density of graphene nucleation sites on the copper surface[70] and by rolling graphene into a cylindrical configuration to prevent excessive copper evaporation[71]. Millimeter-scale graphene grains produced on oxidized copper substrates, yielded electrical properties similar to that of mechanically exfoliated graphene. However, further work is expected to address the improvement of production costs of large-area graphene, due to the energy required to keep the reactor $\geq 1000°C$, which is common with most graphene growth processes. Since graphene growth is approximately linearly dependent on time, new methods are desirable to decrease the graphene growth time of graphene, while maintaining large graphene grains and single-layer uniformity.

Following CVD synthesis of graphene on metal catalyst substrates, it is necessary to remove graphene from the metal substrate in order to transfer graphene to a foreign substrate suitable for applications. Methods for transfer of graphene include dry and wet

etching of underlying metallic substrates[68], heat-treated tape transfer[72], PDMS stamp transfer[73] and the synthesis of graphene directly on dielectric $SiO_2$ using a metal catalyst overlayer[74,75]. A face-to-face method has recently been shown to grow transfer graphene directly on to dielectric substrates without the need for manual transfer[76]. Production of graphene areas up to 30-inch monolayer films (along the diameter) has recently been achieved by a roll-to-roll transfer by thermal release tape for application as a transparent electrode material[77]. However, the sheet resistance of graphene films transferred by the roll-to-roll process is higher than that of the conventional wet etch, PMMA transfer, unless nitric acid is used to electronically dope the graphene. Although electronically doping graphene is an acceptable solution for the application of graphene in transparent electrodes, large-area transfer methods which produce highly conductive graphene without doping are still desirable for other applications.

Wet etching of copper has been one of the most common transfer methods to date, prior to the metal etching process, graphene is often coated by a polymer protective overlayer, such as Poly(methyl methacrylate) (PMMA). Following polymer coating, copper catalyst CVD, copper wet etching process can be performed by a variety of etchants such as iron chloride[63], iron nitrate[68], or ammonium persulfate[77]. Transfer methods have a large effect on the properties and quality of large-area graphene films produced by the copper catalyzed CVD growth method.

Several difficulties arise from the transfer of graphene from CVD growth substrates to dielectric substrates for device characterization. First of all, the introduction

of cracks, tears, and wrinkles may arise from transfer methods involving the manual handling of graphene. For large-area graphene processing, the introduction of any defects or voids will make graphene unable to perform as designed for many applications, causing loss of quality and yield[78,79]. Second, the use of polymers and metal containing etchants to remove metal catalyst layers essentially causes some level of residual contamination to graphene[80]. Most metal species and polymer protective layers used in the CVD synthesis process cause graphene to show p-type electrical doping characteristics. Additionally, charged defects contacting the surface of graphene are shown to decrease the minimum conductivity of graphene[81].

In this work, all graphene was grown by a copper catalyzed CVD growth method and transferred using a PMMA protective layer. The complete CVD process involves a heating ramp up time, copper foil annealing time, graphene growth time, and the CVD furnace cooling time. After loading copper foil substrates into the CVD furnace, the chamber was evacuated by a vacuum pump and then brought up to 5 Torr pressure under $Ar:H_2$ by a digital pressure gauge. The pressure in the furnace was kept at 5 Torr for the remainder of the CVD process. First, a 45 minute heat up ramp up time from room temperature to 1000°C was performed under 10:1 $Ar:H_2$ (50:5 sccm) gas flow. Second, copper foil was annealed at 1000°C for 25 minutes, under the same $Ar:H_2$ flow rate, to smooth the copper foil surface and increase the copper grain size. Smoothing of the copper foil surface improves the uniformity of resulting graphene, causing a higher ratio of single-layer graphene. Larger copper grains results in larger graphene grains, fewer wrinkles and folds. Graphene growth is mediated by flow of methane carbon source gas

at 5 torr. During the graphene growth step, argon was evacuated from the chamber and $H_2$:$CH_4$ gas ratio is 10:1 (20:2 sccm). After 60 minutes the flow of methane was increased to 5 sccm for 5 minutes in order to saturate the copper surface, ensuring complete graphene coverage on the copper foil surface. After the growth process has been completed, methane gas flow was turned off and argon was switched back on so that the samples were kept under 50:5 sccm Ar:$H_2$ gas flow, and the furnace was cooled at a rate of approximately 20° C/min.

Following the CVD growth process, graphene was coated by a PMMA overlayer by spin coating 4% PMMA in anisole at a 2500 rpm rotational rate. After coating, samples were heated on a hotplate at 100°C to harden the PMMA protective layer. Subsequently, samples were placed in air plasma for 2 minutes at medium power, with the PMMA protected side down and the unprotected graphene exposed to plasma. Air plasma causes the unprotected graphene to become damaged and defective, exposing and oxidizing the copper surface. Samples were then floated in 20% nitric acid solution with the air plasma exposed side contacting the acid. This nitric acid step further damages the graphene and etches the copper foil allowing for complete removal of this undesirable graphene. Following nitric acid exposure, samples were placed in 0.1 mM ammonium persulfate solution, overnight, to complete the etching of the underlying copper foil substrate. Graphene samples were then transferred in to deionized (DI) water to dissolve any remaining impurities on the graphene surface before being fished out on to Si/$SiO_2$ substrates and allowed to dry. When no water remains between graphene and the $SiO_2$

substrate, the samples were submersed in acetone solution for 60 minutes to dissolve the PMMA overlayer and rinsed with isopropanol alcohol.

Use of iron chloride or iron nitrate solutions for the etching of copper foil substrates yielded comparatively inferior results. Ideally, CVD produced graphene would exhibit a Dirac point at 0 $V_g$ and with high conductivity. However, the graphene samples transferred with iron nitrate were observed to demonstrate substantial p-type doping behavior. Moreover, graphene samples which were transferred by iron chloride etching solutions were observed to show extreme p-type doping with the Dirac point lying outside the voltage window measurable in the measurement system used in this study. By using nitric acid and ammonium persulfate to remove the copper foil growth catalyst substrate, metallic impurities were greatly reduced since etchants do not contain ionic iron species. Although resultant graphene samples were observed to demonstrate p-type dopant behavior still, this behavior can be attributed to residual PMMA contamination on top the graphene surface, not between graphene and the $SiO_2$ substrate. A field of work has focused on the removal of residual PMMA on transferred graphene by heating in vacuum[80], Ar:$H_2$[82], or $N_2$:$H_2$ environment[83].

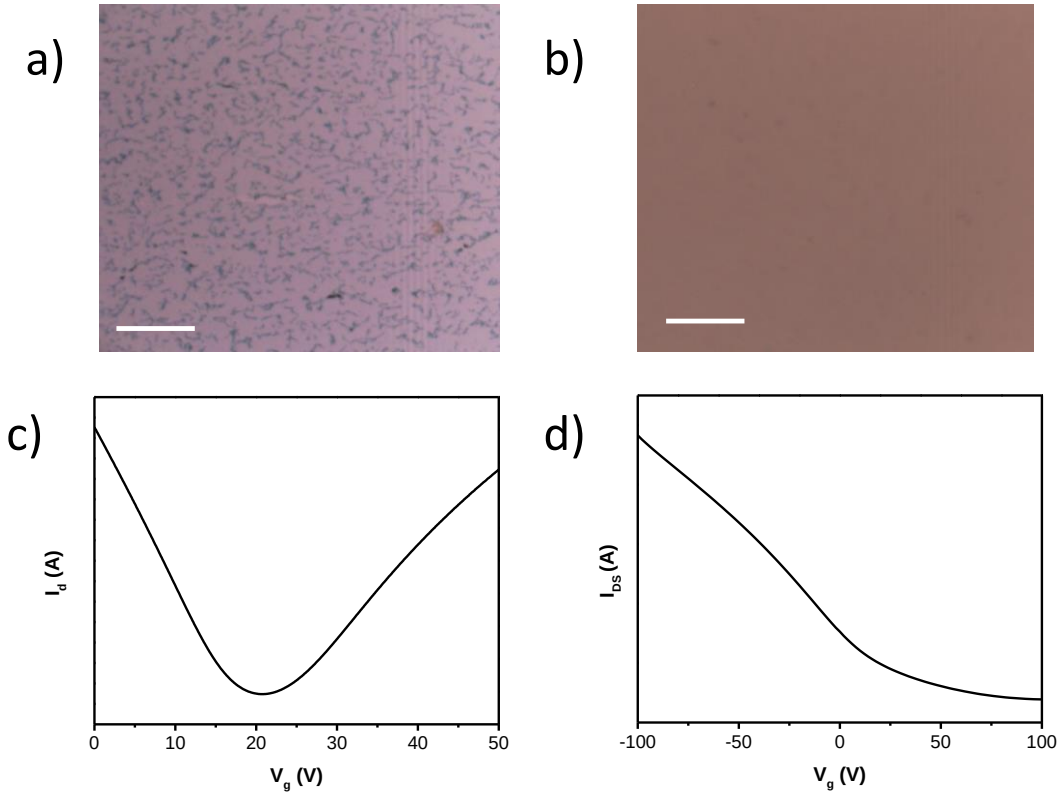


**Figure 8. (**a) Optical image of graphene transferred with ammonium persulfate, using ammonium persulfate and not nitric acid to clean off the undesired graphene. (b) Image of graphene transferred to $SiO_2$ substrate using the nitric acid to clean off the undesired backside graphene. (c) Transfer characteristics of graphene transferred using ammonium persulfate etchant (d) Transfer characteristics of graphene transferred using iron chloride etchant. Scale bars in (a) and (b) are 10 µm.

## 1.4 - Transistors and Integrated Circuits

In 1956, John Bardeen, Walter Houser Brattain, and William Bradford Shockley of Bell Labs were honored with the Nobel Prize in Physics "for their researches on semiconductors and their discovery of the transistor effect"[84]. Early efforts towards transistors focused mainly on Germanium crystals. In 1955 a silicon transistor was developed by Bell Labs. After the commercialization of silicon transistors by Fairchild Semiconductor in 1958, silicon quickly took over the semiconductor industry and has been the major channel material in transistor devices until present. By the 1960s, the integrated circuit was introduced which reduced cost, increased performance, and revolutionized the electronics industry.

In 1965, Gordon Moore, the co-founder of Intel Corporation, described a trend which predicts that the number of transistors in a dense integrated circuit doubles approximately every two years[85]. This trend has become known as Moores's law and has held accurate since 1965 to the present and has been used as a target guide for research and development in the semiconductor industry. Moore's Law is has been a key economic driver in the United States, causing a surge in productivity growth, the primary indicator of economic growth[86]. However, Moore's law has clear boundaries, such as atomic scale miniaturization.

An additional trend in for describing performance of semiconducting devices is Dennard scaling. Dennard scaling suggests that power requirements are proportional to the area of transistors; specifically, performance per watt will grow at approximately the

same rate as transistor density. In combination with Moore's law, this means that performance per watt will roughly double every two years. Dennard scaling is based on the fact that as transistor area decreases, circuits become faster while reducing power consumption per transistor. Based on this calculation, power consumption in an integrated circuit remains the same[87]. Although Moore's law has continued along the predicated trend, Dennard scaling seems to have failed in the past decade, and the performance of integrated circuits has not been able to improve as predicted.

Problems have recently arisen in the scalability of silicon MOSFET technology as a consequence of miniaturization. Short channel effects such as leakage current and an uncontrollable increase of heat have hindered performance progress in the field. Furthermore, electromigation and statistical fluctuations in the channel resistance can become substantial factors in the quality of integrated circuits over time. Furthermore, Rock's law, or Moore's second law, describes a trend that the capital cost of manufacturing products in semiconductor fab increases exponentially over time.

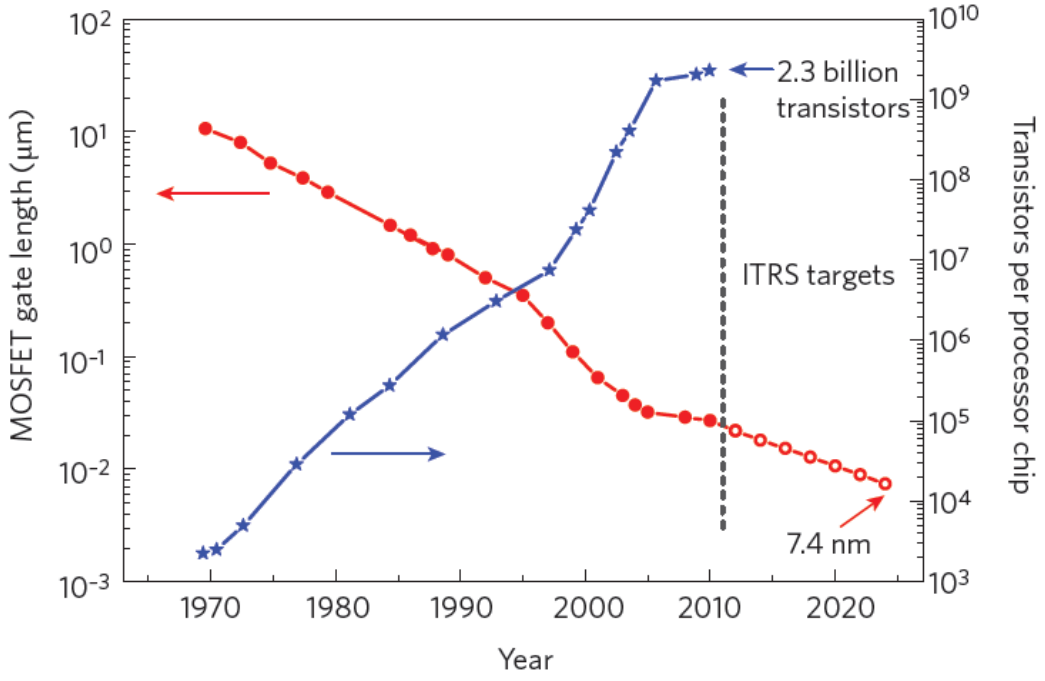


**Figure 9.** Evolution of MOSFET gate length in integrated circuits (filled red circle) and International Technology Roadmap for semiconductor targets (open red circle). The number of transistor per processor is indicated with blue stars[88].

One possible route towards addressing miniaturization problems is by investigating alternative channel materials. Graphene has ambipolar transport characteristics[89], high carrier mobility[1,90], low electrical noise[91], and high thermal conductivity[3], and high cut-off frequency (up to 100GHz)[92]. Nevertheless, graphene is a zero bandgap semiconductor, or semimetal, and therefore, graphene transistors intrinsically show low ON/OFF ratios. A number of approaches have been applied

towards opening a significant electronic band gap in graphene; however, the role of graphene as a material to contribute to meet help fulfill transistor scalability demands is so far unclear.

Flexible thin film transistors are another area of interest which may benefit from the introduction of new channel materials. Polymeric substrates are used for flexible thin film transistors and therefore high temperature processing is not applicable for this application. Thin organic films have been extensively studied for flexible thin film transistors due to their ability to be processed by solution based methods at temperatures near room temperature[93–95]. Despite numerous demonstrations of flexible organic thin film transistors, operation is generally unstable over the long-term and sensitive to operating conditions[96–98].

Due to the short comings in the performance and stability of organic thin film transistors, research has shifted into other flexible transistors of other materials. Inorganic materials of various morphologies have been demonstrated as flexible transistors[99–101]. However, one-dimensional nanowire or nanotube materials are difficult to pattern due to challenges in alignment. Inorganic-organic blends have also been demonstrated as flexible thin film transistors with improved performance[102] and graphene-InGaZnO was also demonstrated as a flexible transistor[103]. In addition to the high conductivity of graphene, graphene is a promising reinforcement material in flexible thin film transistors due to its mechanical properties[63,104–106]. Graphene patterning methods on flexible substrates also make flexible transistors from standalone graphene a promising

approach[107–109]. However, intrinsic lack of band gap in graphene is expected to hinder graphene from a wide range of semiconducting applications for years to come. Graphene will first be applied in flexible display applications according to the graphene roadmap published in 2012[28], and these manufacturing methods will help construct the basis for future commercialization of graphene. Methods for opening a band gap in graphene will be further discussed in Section 3.2.

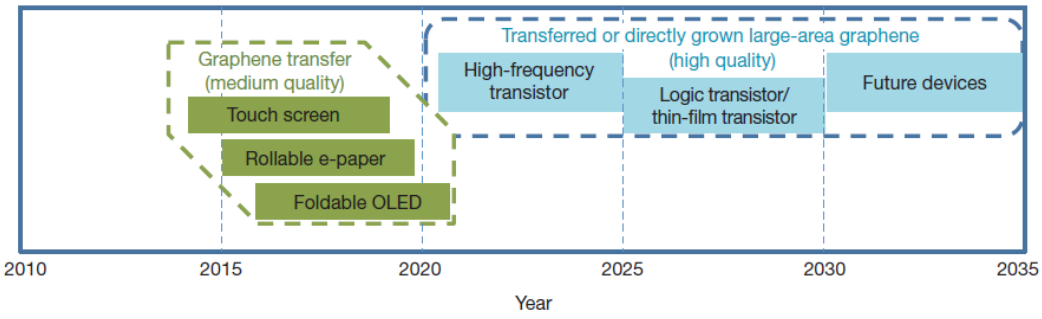


**Figure 10.** Graphene-based display and electronic devices. Display applications are shown in green; electronic applications are shown in blue. Possible application timeline, based on projections of products requiring advanced materials such as graphene. The figure gives an indication of when a functional device prototype could be expected based on device roadmaps and the development schedules of industry leaders[28].

### 1.5 - Introduction to other Two-Dimensional van der Waals Materials

Although solutions for the introduction of graphene into the enormous semiconductor field as a channel material may be an insurmountable task, the discovery

of graphene has sparked extraordinary interest in two-dimensional van der Waals materials. Unlike graphene, many other van der Waals materials possess substantial band gaps and are promising candidates to enter transistor applications as channel materials. Numerous of van der Waals materials exist and remain to be studied with the intensity that graphene has been studied thus far. It is worth noting that this family of two-dimensional van der Waals materials refers to materials which are thinned down to one layer, or one unit cell thickness, and does not apply exclusive to one atom thick layers.

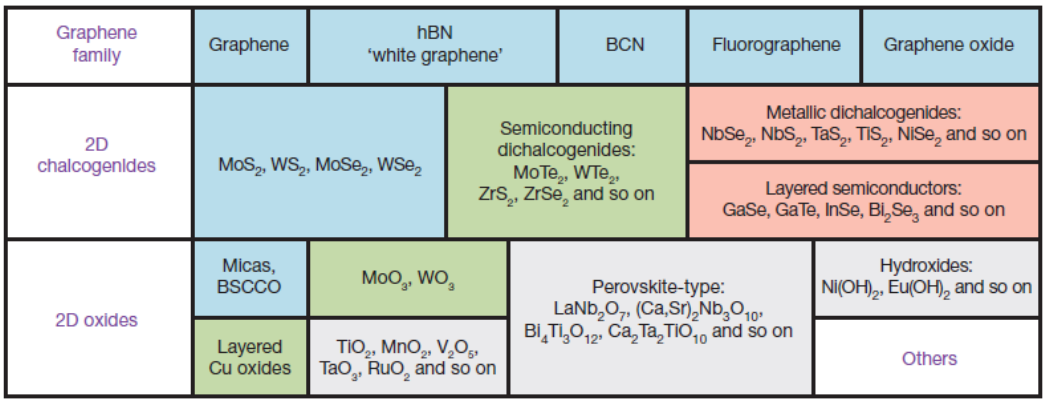


**Figure 11.** Current 2D library. Monolayers proved to be stable under ambient conditions (room temperature in air) are shaded blue; those probably stable in air are shaded green; and those unstable in air but that may be stable in inert atmosphere are shaded pink. Grey shading indicates 3D compounds that have been successfully exfoliated down to monolayers, as is clear from atomic force microscopy, for example, but for which there is little further information[110].

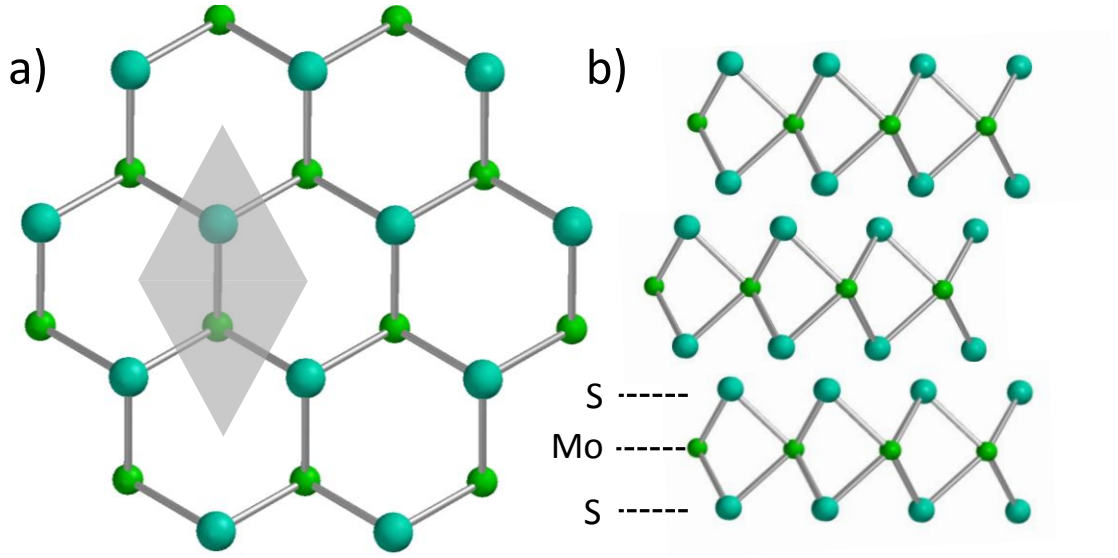


**Figure 12.** Molybdenum Disulfide. Grey-shaded area indicates the primitive unit cell. The hexagonal spacing of like-atoms is 3.17 angstroms and Mo-S bond length (extending out of plane) is 2.42 angstroms. $MoS_2$ adopts an ABA stacking similar to graphene.

Molybdenum disulfide is a van der Waals material in which each layer consists of a sulfur-molybdenum-sulfur stack. The interlayer spacing between each S-Mo-S stack is approximately 6.5 angstroms[111]. Similar to graphene, electronic band structure properties of $MoS_2$ are altered substantially when the material reduced down to single-layer thickness. $MoS_2$ is a semiconducting phase transition metal dichalcogenide material which possesses an indirect bandgap of approximately 1.29 eV in bulk form. When separated into a single-layer the band diagram is shifted, revealing a direct bandgap of

approximately 1.8 eV[112,113]. $MoS_2$ is classified as a member of the transition metal dichalcogenide (TMD) family. TMDs are a class of materials with the formula MX2, where M is a transition metal element from group IV, group V, or group VI, and X is a chalcogen (S, Se or Te). It is characteristic of TMDs to have the X-M-X layered structure and several other materials in this family have an indirect to direct band gap transitions at atomic layer thicknesses, similar to $MoS_2$. Further discussion about TMD synthesis and applications can be found in chapter 4.

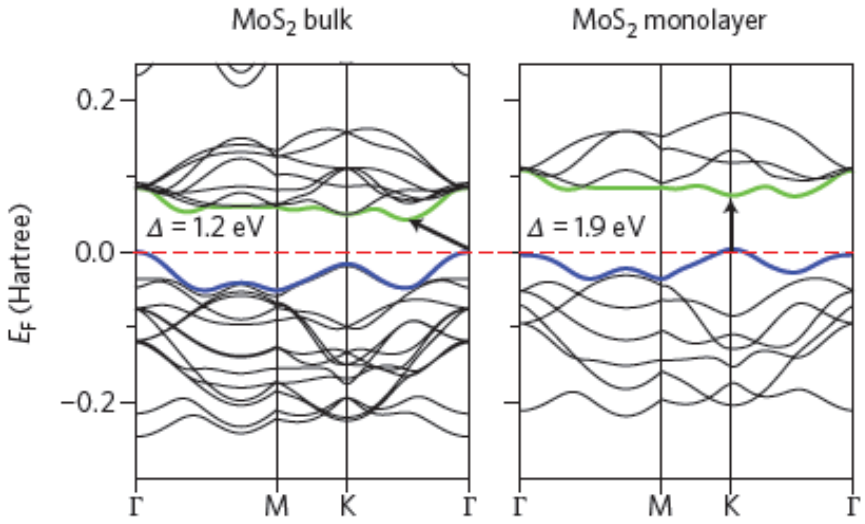


**Figure 13.** Band structures calculated from first-principles density functional theory (DFT) for bulk and monolayer $MoS_2$. The horizontal dashed lines indicate the Fermi level. The arrows indicate the fundamental bandgap (direct or indirect). The top of the valence band (blue) and bottom of the conduction band (green) are highlighted[114,115].

By definition, van der Waals materials feature weak interlayer bonding. Mechanical exfoliation is an assured method to produce many van der Waals materials down to single layer thickness. Similar to graphene, customized chemical exfoliation and CVD approaches may also be applied to many other van der Waals materials. An arising field of research in two-dimensional van der Waals materials is the study of van der Waals heterostructures. Through van der Waals heterostructures, different individual layers may be matched to yield the advantageous material properties of each individual material. For instance, hexagonal boron nitride (h-BN) is a two-dimensional material composed of boron and nitrogen in a hexagonal pattern, with a sizable direct band gap of almost 6 eV[116]. When h-BN is used as a dielectric for graphene devices the mobility of graphene is greatly enhanced over that of graphene on $SiO_2$ dielectrics[90,117]. Device improvement may be attributed to the atomic smoothness, absence of dangling bonds, and the excellent lattice matching of h-BN to graphene. Future research will assuredly investigate the effects of interactions between van der Waals materials and a wide range of other materials in the search to tailor material properties to various applications.

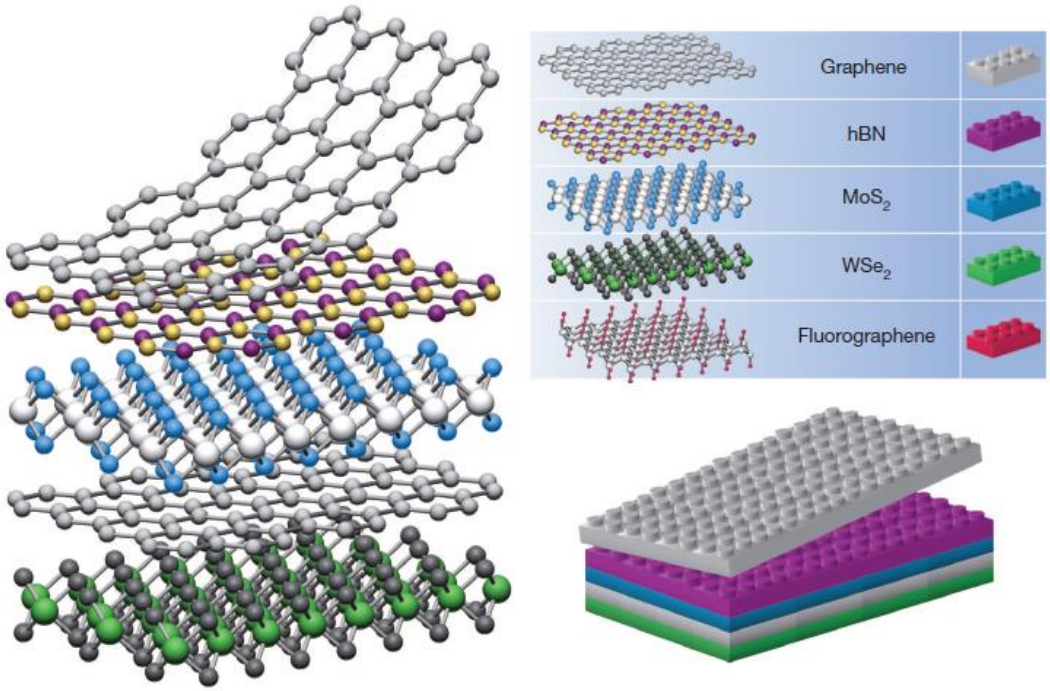


**Figure 14.** Building van der Waals heterostructures. If one considers 2D crystals to be analogous to Lego blocks (right panel), the construction of a huge variety of layered structures becomes possible. Conceptually, this atomic-scale Lego resembles molecular beam epitaxy but employs different 'construction' rules and a distinct set of materials[110].

# Chapter 2 - Interactions Between Zwitterionic Polymers and Graphene

## 2.1 - Graphene surface interactions and challenges in graphene electronics

Due to large surface to volume ratio of graphene materials, substrate and overlayer interactions can cause significant changes in graphene field-effect transistor (FET) performance. Interactions between zwitterionic polymers and graphene materials systems are studied in different transistor configurations. In this chapter, possibilities of changing the doping, carrier concentration, and contact resistance of graphene FETs through surface interactions with zwitterionic polymers were studied.

Intrinsic electrical properties such as ballistic transport and high mobility, suggest that the remarkable qualities of graphene may be used in several future electronics applications[9,24]. Surfaces contacting graphene have substantial effects on these properties. Graphene surface interactions are particularly interesting due to the large effect surface absorbents have on the electrical characteristics of graphene[81]. Understanding the nature of these interactions can allow for accurate tuning of charge carrier concentrations and is of significant scientific importance. Suspended graphene devices and graphene devices with one-dimensional contact have been shown to have drastic improvements over graphene devices on $Si/SiO_2$ substrate[90,118]. Modulation of charge carrier concentration by impurities is indicated by the shift of the Dirac point and variance of electron and hole mobilities[119–122].

In graphene electronics, graphene-metal interactions impose a limit on electrical properties such as maximum drive current[123,124]. However, graphene lacks surface bonding sites and strong orbital hybridization, leading to high contact resistance[125,126]. The work function and nature of graphene under various metal contacts has also been studied and by a variety of methods[127,128]. Thin interlayers have previously been shown to provide improved device performance in organic devices[129–131]. Improved performance of thin interlayers may be explained by modification of surface wettability or modification of electronic states at the interface. Zwitterionic polymers are an interlayer material of interest due to their ability to modify the work functions at the organic-metal interface due to dipole alignment[132].

Thin films of conjugated sulfobetaine-containing polymeric zwitterions were studied as a graphene-metal interlayer for graphene FETs. Specifically, conjugated sulfobetaine-containing polymeric zwitterions with sulfobetaine-substituted polythiophene backbones (PTSBMA) and alternating thiophene−benzothiadiazole (PTBTSB-2) backbones[133,134]. Characterization of these interlayers was carried out by ultraviolet photoelectron spectroscopy (UPS), transfer length measurements (TLM), near edge x-ray absorption fine structure spectroscopy (NEXAFS) measurements.

Graphene samples were prepared by CVD growth on copper foil substrates by methane source gas[68]. Following synthesis, films were transferred to silicon substrates with 300 nm of thermal oxide by PMMA-mediated transfer using ammonium persulfate etchant.

## 2.2 - Properties of Conjugated Zwitterionic Polymers

The operation of organic electronic and optoelectronic devices relies on the electronic characteristics between the organic active layer and the electrode. Interlayers have been shown to improve performance in polymer light-emitting diodes[135], solar cells[136], and organic thin-film transistors[131].

Explanation of the positive effect of interlayers range from improved surface wettability and adhesion to morphological optimization and electronic structure modifications. Close proximity of the sulfobetaine groups to the polymer backbone results in high ionization potential and band gaps of 2.04 eV for PTBTSB-1. This ion motion can redistribute the electric field when used as an interlayer in a device structure.

Conjugated polymeric zwitterions (CPZs) may cause a modification in the work function of contacting materials by surface dipole alignment. To investigate the possible effects of surface dipole alignment, ultraviolet photoelectron spectroscopy (UPS) is carried out on graphene and gold, before and after the coated of thin CPZ layers. Figure 15 shows work function values as a function of CPZ concentration in solution. Work function values for both graphene and gold are perceptibly altered as the CPZ concentration is increased due to the presence of interfacial dipoles. For PTSBMA, work functions of graphene and gold change from 4.59 to 2.86 eV, and 4.78 eV to 3.26 eV, respectively. Pyrene-containing PTSBMA (PTSBMA-Py) was also characterized by UPS due to the improved wettability of pyrene on the hydrophobic graphene surface. A PTSBMA-Py (50% Py) layer similarly shows substantial reduction of the work function of graphene, lowering the work function by 1.29 eV.

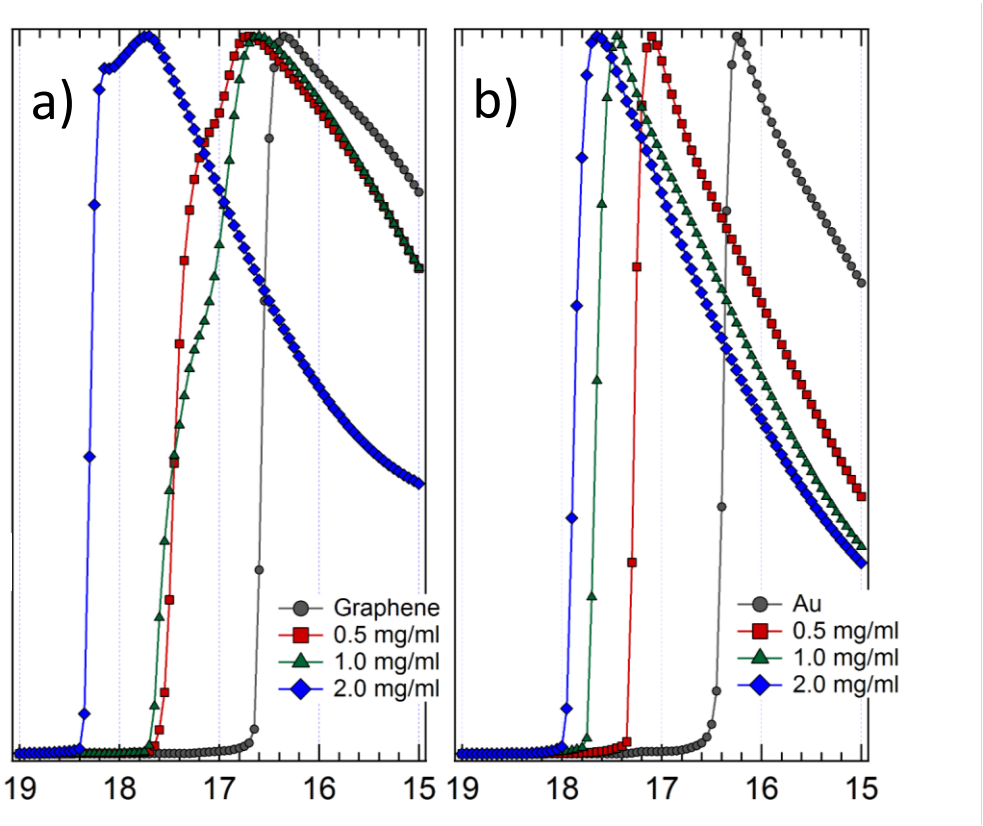


**Figure 15.** Work function modification by UPS measurements of (a) graphene and (b) gold layers.

NEXAFS spectra (Figure 16) were used to access orientation at different average depths by Carbon K-edge total electron yield (TEY, ≈10 nm) and Auger electron yield (AEY, ≈1 nm). NEXAFS characterization of spin coated CPZs reveals that at low concentrations, CPZ layers may not completely cover the underlying graphene surface, as evidenced by C 1s $\sigma_1$ and $\sigma_2$ transitions[137,138]. As concentration and thickness are increased, C 1s $\sigma_1$ and $\sigma_2$ transitions are obscured, while C 1s $\pi_1$ and $\pi_2$ peaks remain

apparent. Further analysis reveals that reveals PTSBMA-Py (10% Py) shows dipole orientation with the pyrene-group face-on the graphene surface.

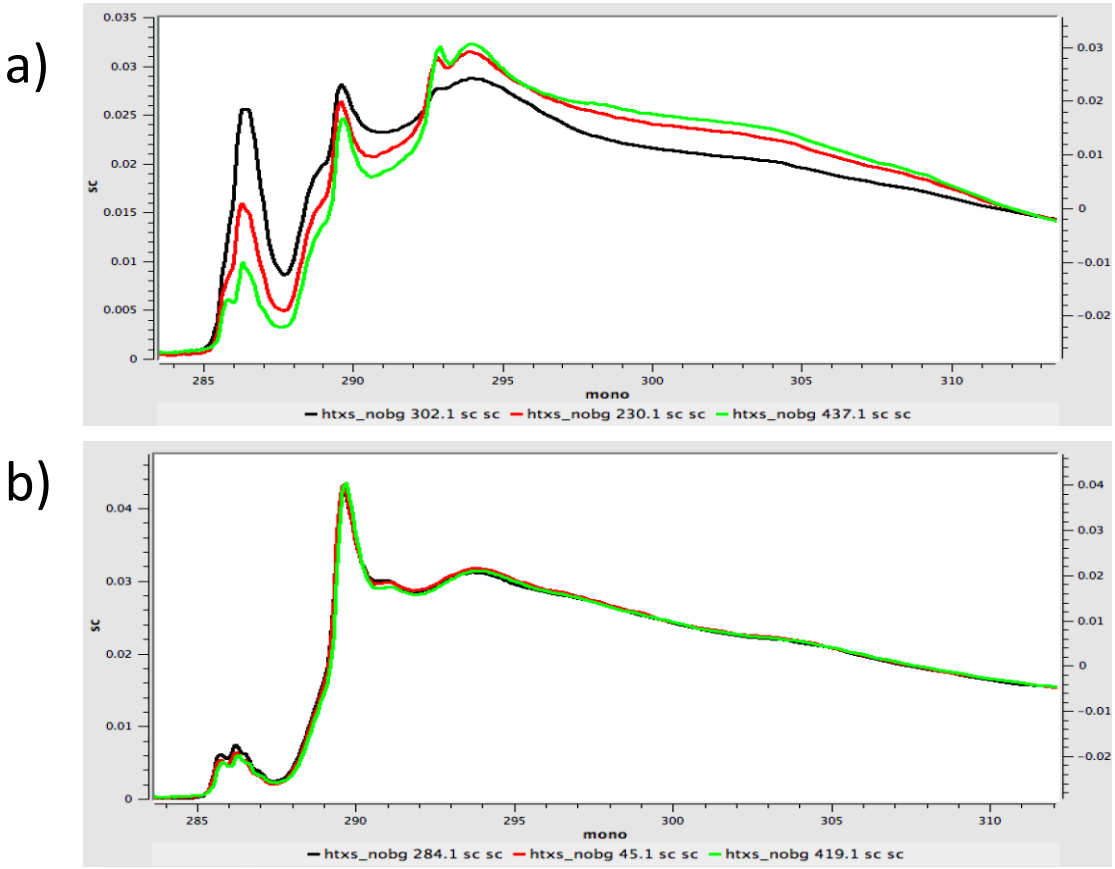


**Figure 16.** NEXAFS of graphene with (a) 5 nm of PSBMA-Py (10%) and (b) 15 nm of PSBMA-Py (10%).

## 2.3 - Lowering the Contact Resistance of Graphene Devices

Back gate graphene transistor characteristics offer further insight into the nature of the graphene-CPZ-gold contact. Prior to Au metal deposition for graphene device measurements, sulfobetaine (SB)-containing polymeric zwitterions (CPZs) PTBTSB-2 and PTSB-Py were spin coated on to graphene thin films. Fabrication of graphene FETs was carried out by evaporating 80 nm gold through a shadow mask with variable contact spacing. Two-probe TLM measurements shown in Figure 17 were used to obtain the contact resistance of fabricated devices. The greatest improvement in contact resistance was found using concentrations of 0.5 and 0.75 mg/mL, for PTSBMA-Py and PTBTSB-2, respectively. For monolayer graphene, the contact resistance of gold was decreased from 155.2 Ω to 98.9 Ω using PTBTSB-2 at 0.75 mg/mL. PTSBMA at 0.5 mg/mL allowed for a reduction of the contact resistance from 155.2 Ω to 114.0 Ω. Longer conjugated backbone chains may attribute to an increased ability to cause greater dipoles, increasing band bending between the two materials and lowering the contact resistance.

The reduction of the contact resistance may be due to (1) improved wettability and adhesion of gold contacts to the underlying graphene layer and (2) decreasing the difference in work function between graphene and gold contacts. Unlike in the case of Cr/Au or Ni contacts, determination of the work function of graphene under a Pd and Au electrodes has shown that the work function of graphene is unchanged (~4.6 eV)[139]. It should be noted that the work function of PSBMA on graphene and gold is closest at around 1 mg/mL when measured separately on each material. Although dipole interactions at the interface will not behave as in the case of each individual substrate,

this concentration value is close to the optimal value used to lower contact resistance. Additionally, NEXAFS characterization of CPZ coating on the graphene surface indicates that the polymer does not fully cover the graphene surface, indicating the effect of graphene-gold adhesion may be less significant.

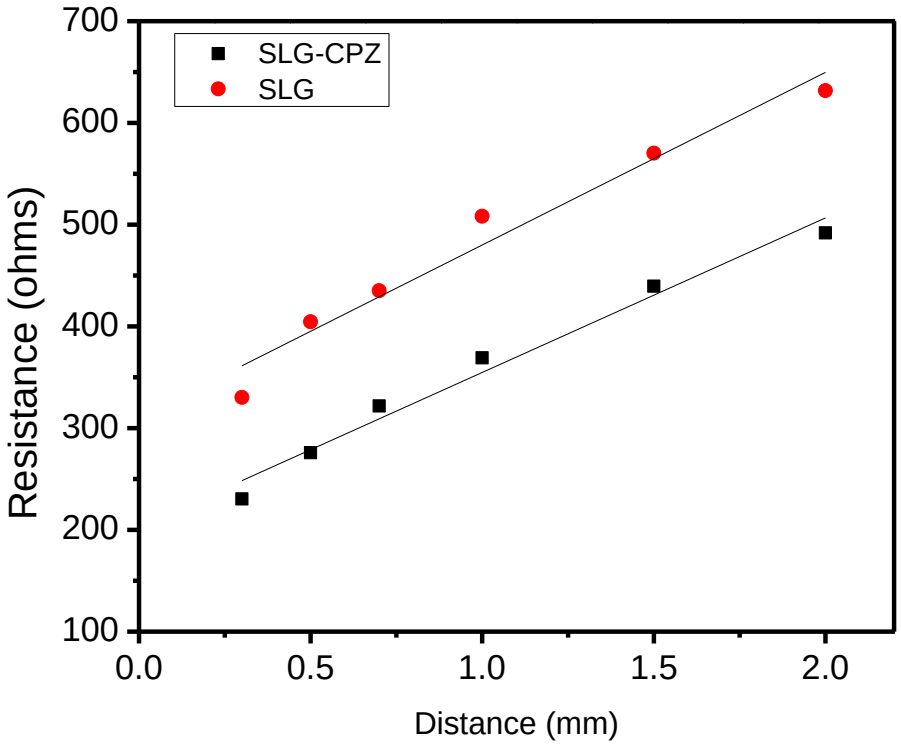


**Figure 17.** Transmission line measurement of graphene-gold devices with (black) and without (red) zwitterionic interlayers.

In summary, CPZ interlayers were shown as a means to lower contact resistance in graphene transistor applications. Contact resistance can be lowered by as much as 64% in a graphene-CPZ-gold configuration. CPZ interlayers offer contact resistance lowering

without substantially changing the carrier concentrations in graphene. Interlayers used here may be useful in lowering the contact resistance in various other systems, increasing maximum performance in ferromagnetic and solution-processed contacts.

# Chapter 3 - Block Copolymer Ordering on Graphene for Fabrication of Graphene Nanomesh

## 3.1 - Introduction to Block Copolymers and Block Copolymer Lithography

Block copolymers (BCPs) are materials in which polymeric chains composed of distinct monomers are joined together. The use of BCPs allows the user to utilize the physical properties of each distinct monomer. Diblock, triblock, and multiblock polymers have been synthesized, in which each monomer chain is termed a block. Polymerizations of BCPs are mainly performed by the synthesis methods of anionic polymerizations and living radical polymerization[140]. Ambiphilic BCPs have attracted a large degree of interest in the scientific community due to their ability to self-assemble into ordered morphologies on the nanoscale. This self-assembly is made possible due to the microphase separation of polymeric blocks, detailed by Leiber in 1980[141]. By this property, BCPs address the current obstacle in nanotechnology for lithography at the few-nanometer range. Various periodic morphologies such as spherical[142], lamellar[143], and cylindrical[144] domains have been experimentally obtained due to the separation of properly selected length blocks.

Theoretical studies[145,146] as well as experimental studies[147,148] have investigated the effects of electric field strength, interfacial energies, film thickness, dielectric constant differences, and commensurability of the film thickness and the natural period of the copolymer. This method opens an opportunity to achieve different morphologies with

good ordering by the application of an external electric field. Addition of a homopolymer to diblock copolymer solution has been studied as a way to increase the thickness of BCP films[149]. Nanoporous BCP templates have been achieved with the addition of homopolymer since the homopolymer can be selectively rinsed away[150]. A variety of methods for surface reconstruction of BCP templates exist due to differences in the physical properties of the distinct polymeric blocks.

A solvent annealing process for improved cylindrical ordering of BCP thin films by solvent vapors has been employed and described by Kim et. al.[151]. In this process, smooth substrates covered with a thin layer of BCP are put in a sealed container and exposed to solvent vapor. Critical parameters for the described procedure have been shown to be film thickness, vapor pressure, temperature, and exposure time. Other BCP patterning processes feature the use of electric fields to control the ordering of domains.

Self-organization of block copolymers provides an attractive method for several areas of science and technology which require the inexpensive fabrication of well-ordered arrays at the nanoscale. Chemical differences between the two ambiphilic blocks of diblock copolymers allow for the selective alteration of each block and the attachment of a wide variety of species to produce periodic nanoscale features. Lithography methods by BCPs have found multiple applications in nanotechnology. Diblock copolymers have been demonstrated for patterning by top-down etching processes as well as bottom-up fabrication of nanoparticles[152,153], nanopillars[154], and nanorings[155,156].

Surface reconstruction of BCPs has opened the door for the fabrication of materials in different morphologies. Partial or complete removal of one of the polymer blocks can be achieved by taking advantage of chemical differences between the polymer species. Selective surface reconstruction of the PVP block is achieved by dipping BCPs in alcohol[155], vapor exposure of methanol and/or ammonia[156], or by chemical exposure creating pH imbalance. Deposition of virtually any material into nanoporous BCP templates can be used to pattern well-ordered nanoparticles and nanopillars[157]. Moreover, surface reconstructed BCP templates may be used as a hard mask for the etching of underlying materials.

### 3.2 - Semiconducting Graphene by Quantum Confinement

Opening of an electronic band gap in graphene has been observed by etching graphene into one-dimensionally nanoscale confined sheets, or graphene nanoribbons.[46] Graphene nanoribbons have been fabricated by a variety of synthesis methods. Graphene nanoribbons can be formed from graphene starting material using electron beam lithography methods and etching undesirable graphene regions by plasma etching[158]. Plasma etching of graphene by argon or oxygen plasma produces rough edges containing $sp^3$ bonding sites[159]. Graphene edge type plays a significant role in the band gap formation in graphene nanoribbons[159].

A few different methods have been shown for the fabrication of graphene nanoribbons. Graphene nanoribbons on SiC were fabricated using scalable templates[160].

Graphene nanoribbons were grown directly from nickel nanobars using rapid-heating plasma enhanced chemical vapor deposition[161]. Other methods towards graphene nanoribbon synthesis involve the use carbon nanotubes as a starting material. Multiwalled carbon nanotubes were oxidized stepwise oxidization in $KMnO_4$ and $H_2SO_4$, then reduced and "unzipped" to produce graphene nanoribbons in $NH_4OH$ and hydrazine in $N_2H_4.H_2O$ solution[162]. Another chemical opening of multiwalled carbon nanotubes was achieved by lithium and ammonia intercalation followed by sonication in acid and rapid heat treatment[163]. An alternative graphene nanoribbon synthesis approach involving carbon nanotubes was performed by etching carbon nanotubes partially embedded in PMMA by Ar plasma[164]. All graphene nanoribbons with diameters less than 10 nm show semiconducting behavior, although scattering events in graphene nanoribbons substantially reduce mobility[165,166].

Even though graphene nanoribbons with widths of less than 10 nm have shown substantial ON/OFF ratios, the current and conductance of individual graphene nanoribbons is too low for many applications. To obtain higher currents in semiconducting FETs a network of graphene nanoribbons should be utilized, or graphene nanomesh (GNM).

### 3.3 - Graphene Nanomesh Fabrication

Graphene nanomesh was fabricated by Bai et al which demonstrated substantial ON/OFF current ratios and current magnitudes nearly 100 times larger than individual

graphene nanoribbons[167]. Graphene oxide has been etched into a GNM configuration by multiple methods[168–170]. However, chemical methods to isolate and reduce graphene oxide sheets produce multilayer sheets and inconsistent geometries over large areas. Chemical vapor deposition (CVD) has been shown to produce uniform single-layer graphene on copper substrates[68]. Large-scale single-layer graphene produced by CVD with dimensions of up to 30-inches along the diameter has been demonstrated by a roll-to-roll transfer method[77]. Furthermore, graphene produced by CVD offers reproducible chemical and electrical properties.

In this work, the fabrication of GNMs was shown by patterning of a poly(styrene)-block-poly(4-vinylpyridine) (PS-b-P4VP) block copolymer (BCP) templates directly on graphene via solvent annealing[171]. This technique is advantageous for multiple reasons. First, the use of toxic gases ($SF_6$, $CHF_3$, $CF_4$) and HF was avoided. The avoidance of these chemistries is critical as they may cause defects in the $SiO_2$ layer, affecting device performance. Second, this technique reduces the number of process steps and the necessity for any interface materials between graphene and the BCP etching mask. Third, superior control over graphene neck sizes can be achieved due to the position of the BCP etching mask template directly on top of graphene.

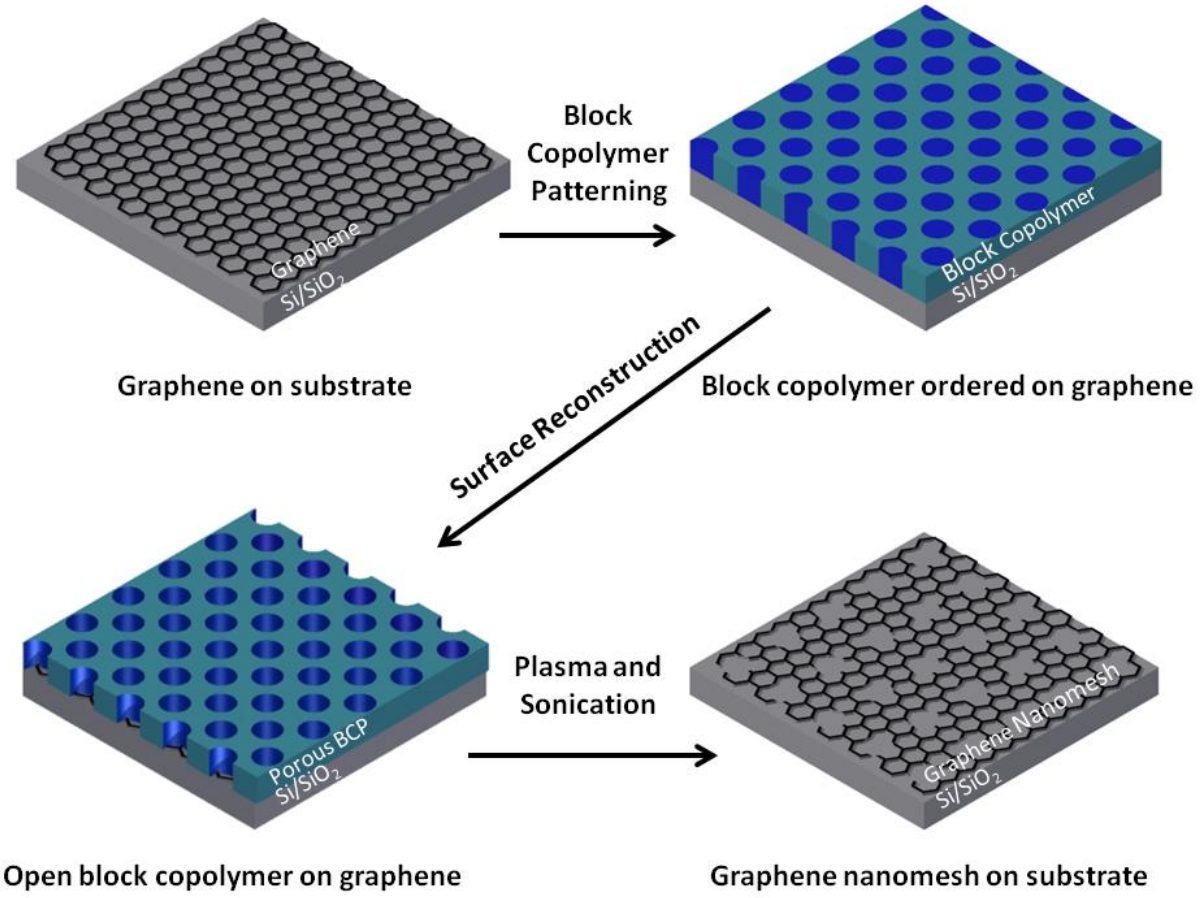


**Figure 18.** Schematic illustration of graphene nanomesh fabrication using PS-b-P4VP block copolymer templates directly on CVD grown graphene.

Graphene was grown by a CVD furnace on copper foils at 1000$^{o}$ C under the flow of $CH_4/H_2$ at a ratio of 1:4 at 20 Torr. Before the introduction of the source gases the Cu foil was ramped to 1000$^{o}$ C and annealed under $Ar/H_2$ at a ratio of 2:1 for 25 minutes. The continuous graphene sheets were transferred on to $Si/SiO_2$ substrates, completing the graphene synthesis process. Thin BCP films were spin coated directly on to the graphene

layer from a 0.7 weight % 69 kg/mol PS-b-P4VP in 4:1 toluene:tetrahydrofuran solution. After spincoating deposition, samples were placed inside of closed containers in the presence of tetrahydrofuran vapor to increase mobility and improve the ordering of BCP thin films. Following a solvent annealing process, BCP thin films with hexagonally close packed vertically aligned domains were observed by atomic force microscopy (AFM). Surface reconstruction of PS-b-P4VP BCP thin films was performed as previously shown[155,172].

Copper substrate prepared CVD graphene demonstrated excellent layer uniformity. The smooth graphene substrate allows deposition of consistent BCP thickness, leading to the preparation of hexagonally ordered cylindrical BCP templates. Moreover, monolayer graphene may be advantageous due to the minimal effect on surface wettability[173,174]. A generalized approach to surface modification with was performed by Du Yeol Ryu et al.[175]. However, the random copolymer was insoluble, making it difficult to remove. In this work, it was demonstrated that for monolayer CVD synthesized graphene no surface modification was necessary to obtain well ordered BCP patterns. Other polymer systems and morphologies may be realized by patterning BCP templates directly on graphene. Patterning of hexagonally patterned photocleavable BCPs[176] would allow monomer removal from the graphene surface with less vigorous methods.

Reactive ion etching (RIE) was used as a means to widen the pores in the BCP thin films and etch the underlying graphene films into the desired GNM structures.

Plasma composed of oxygen/argon at 9:1 ratio was used in this work to widen the pores, similar to that shown by Gu et. al.[177,178]. Argon was necessary to the gas mixture to add an aspect of ion bombardment on the BCP surface, widening and delaying the closing of pores. Without argon, the BCP pores will close after prolonged exposure and to return to the original hexagonally ordered pattern.

Careful consideration is needed in order to etch the pattern of the BCP template into the underlying graphene layer. Some of the PVP block may not be completely removed from the cylindrical domains of the BCP template and would therefore need to be etched away by plasma exposure before the underlying graphene can be etched. On the other hand, the thickness of the BCP layer is gradually decreased over increasing etching time and overexposure will destroy all underlying graphene. To study the effects of RIE on BCP templates over time, ordered BCP thin films on $Si/SiO_2$ substrates were prepared by solvent annealing. Following BCP patterning, a surface reconstruction was performed by submerging substrates in ethanol for 20 minutes. Ethanol exposure caused the PVP block to swell and become displaced from the confinement of the cylindrical domains, leaving pores in the BCP film.

After surface reconstruction, the effect of RIE plasma time on the BCP etching template was studied as a progression of time. As shown by AFM in Figure 19, the pores in the BCP template are widened as a function of time, up to approximately 30 seconds. After 45 seconds of RIE plasma treatment, a small amount of polymer remains on the

$Si/SiO_2$ surface, suggesting the polymer layer was removed at approximately this treatment time.

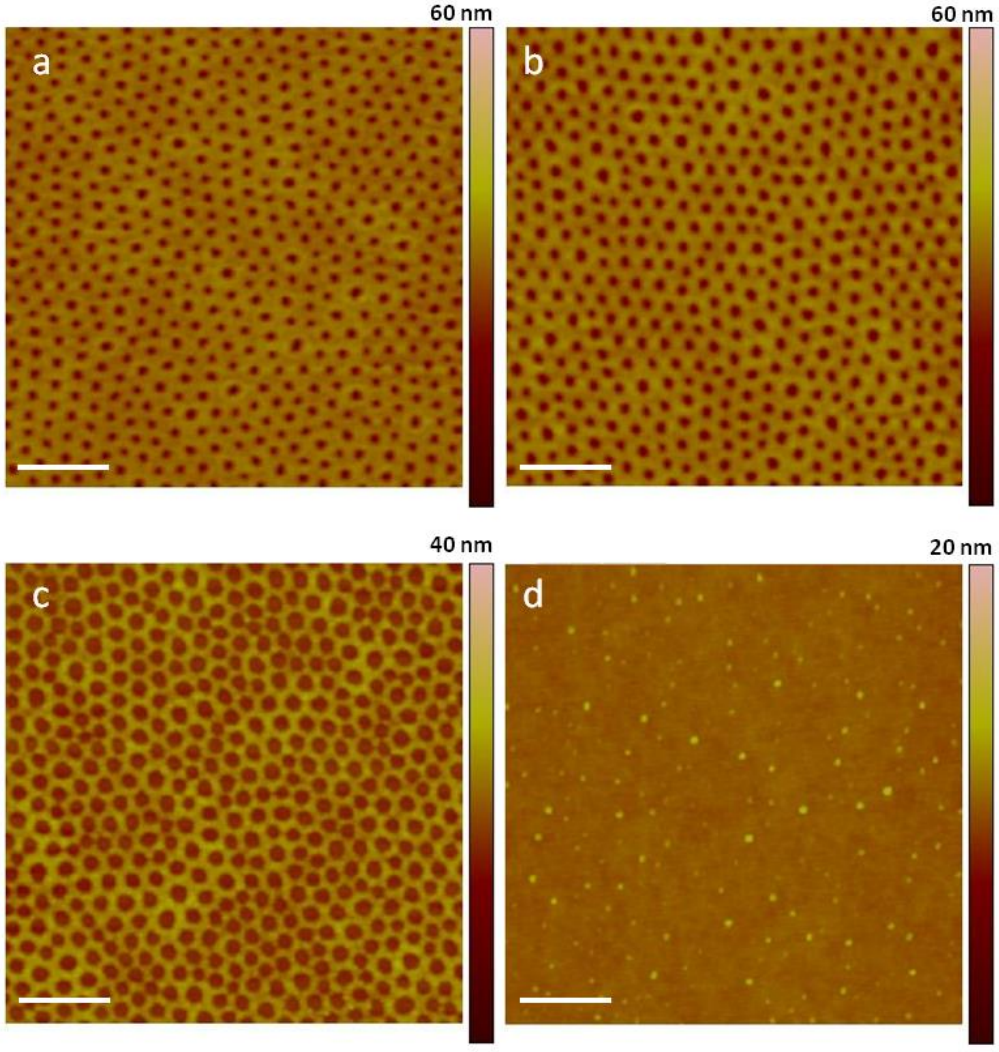


**Figure 19.** Progression of pore widening as a function of plasma treatment time on $Si/SiO_2$ wafers. Plasma treatment times correspond to the AFM images above as: (a) 10 sec (b) 20 sec (c) 30 sec (d) 45 sec. Scale bars in all images are 200 nm.

Pore size and spacing can be controlled by BCP molecular weight. Figure 20 demonstrates the morphology of 69 kg/mol PS-b-P4VP (a-c) and 32 kg/mol PS-b-P4VP BCP (d-f) on graphene by AFM after patterning, surface reconstruction, and 30 seconds of RIE plasma treatment. By decreasing the molecular weight of the BCP is shown to yield smaller, denser pores.

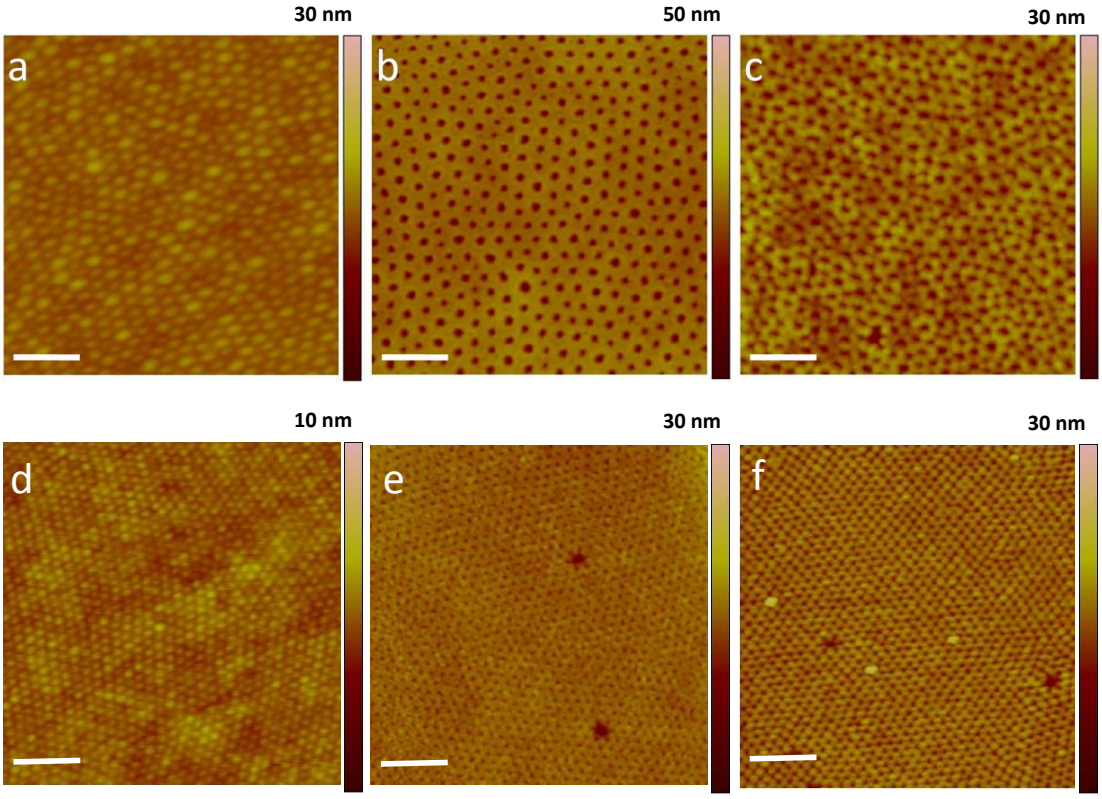


**Figure 20.** AFM scans of 69 kg/mol PS-b-P4VP on graphene after (a) solvent annealing (b) surface reconstruction and (c) after plasma treatment. Similarly, 32 kg/mol PS-b-P4VP on graphene after after (d) solvent annealing (e) surface reconstruction and (f) after plasma treatment. Scale bars in all images are 200 nm.

Upon removal of the BCP template by sonication in toluene, scanning electron microscopy (SEM) was used to image the morphology of the resulting GNM structure. SEM image of the obtained GNM, shown in Fig. 2, shows GNM with hole to hole spacing of 50-60 nm and neck widths of approximately 10 nm. Comparison between AFM of the BCP template and SEM of the resulting GNM structure suggests that the plasma conditions minimally underetch the BCP etching template.

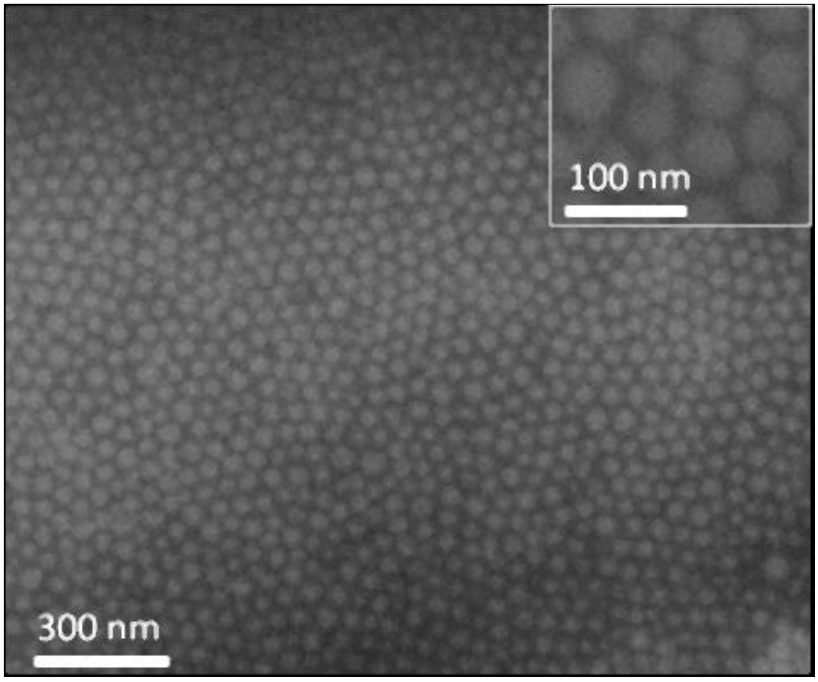


**Figure 21.** SEM image prepared GNM showing graphene neck sizes with width of approximately 10 nm.

GNM patterning by BCP ordering directly on graphene can be applied to CVD prepared graphene as well as to exfoliated graphene flakes. The procedure for exfoliated graphene is similar to that of CVD graphene. Characterization of multilayer exfoliated graphene and single-layer graphene produced by CVD demonstrates that multilayer graphene can be patterned into graphene nanomesh, as well as single or few layer graphene. Raman spectroscopy is a widely used tool in understanding the quality and electrical properties of graphene[34,179]. Raman spectroscopy of GNM was previously reported experimentally, showing an increase in the D peak due to the increased percentage of edge states[168,180]. Measurement of the D peak may prove to be an important measurement due to the energy gap dependence on defects as well as graphene neck width, and the type of defect[181]. GNM morphologies can be compared to a network of graphene nanoribbons. In this report, phenomenon in GNMs are similar to those which have been observed in previous Raman spectroscopy studies of graphene nanoribbons[182].

Importantly, a large increase in the D peak intensity (~1350 $cm^{-1}$) was observable after plasma etching and consequently, an increase in the $D^*$/G peak ratio. A redshift in the G peak was observable in graphene nanomesh, suggesting p-type doping[122]. Stiffening of the G peak was observable due to the nonadiabatic removal of the Kohn anomaly from the $\Gamma$ point[27]. The G/2D peak ratio was increased by the doping effect by introducing defects in the graphene lattice. Although the G/2D peak ratio has often been used as an indicator of the number of layers in graphene samples[36,183], it is important to note that the G/2D peak ratio is strongly dependent on the carrier concentration in graphene samples[184].

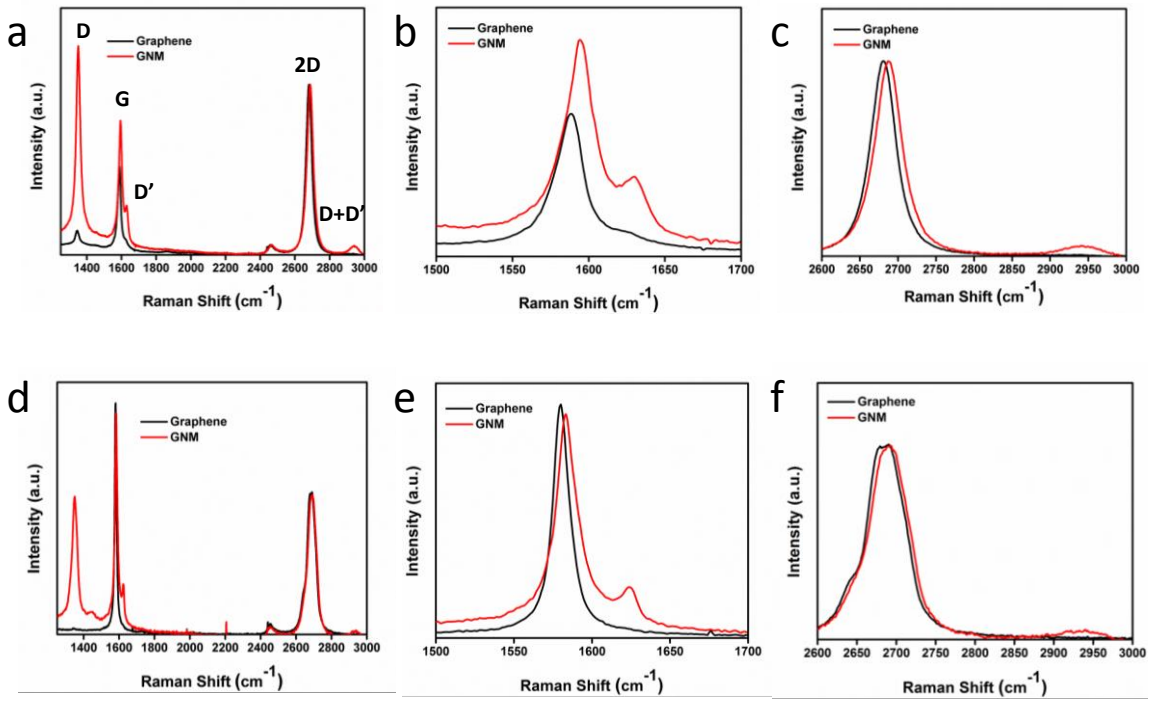


**Figure 22.** Raman spectroscopy of graphene prepared by (a-c) CVD synthesis and (d-f) exfoliation. Features include the emergence of a (a,d) high intensity D peak, (b,e) redshift and stiffening of the G peak, emergence of the D' peak, and (c,f) redshift of the 2D peak and the appearance of a small D+D' peak.

To evaluate the properties of the GNM devices, back-gate field-effect transistors (FETs) were fabricated $Si/SiO_2$ substrates using a conventional photolithography method to pattern Ti/Au (10/80 nm) electrodes (Figure 23). The ON/OFF current ratio of CVD graphene devices was found to be approximately 1.9, while the ON/OFF current ratio for CVD GNM devices was increased to approximately 6.7. Field-effect mobility was extracted using the equation $\mu=(\Delta Id/\Delta Vg)/(\varepsilon VdW/L_{ox}L)$, where $L_{ox}$ is oxidation thickness

(300 nm), L is the length of the channel, W is the channel width, ε is the gate dielectric ($\varepsilon_{SiO2}$ = 3.9), and ($\Delta Id/\Delta Vg$) is the slope calculated from Fig 3. Mobility of GNM decreased by a factor of six times compared to that of unpatterned graphene layers, due to the introduction of a large number of defects into the graphene structure. Defect sites in the produced GNM structure are likely inhabited by $sp^3$-bonding oxygen species due to the use of oxygen plasma etching of the GNM structure. The effect of the functionalized graphene edges causes the GNM to show p-type doping behavior since oxygen is more electronegative than carbon. Moreover, the edges of graphene formed by oxygen plasma are likely to be highly disordered atomically[185].

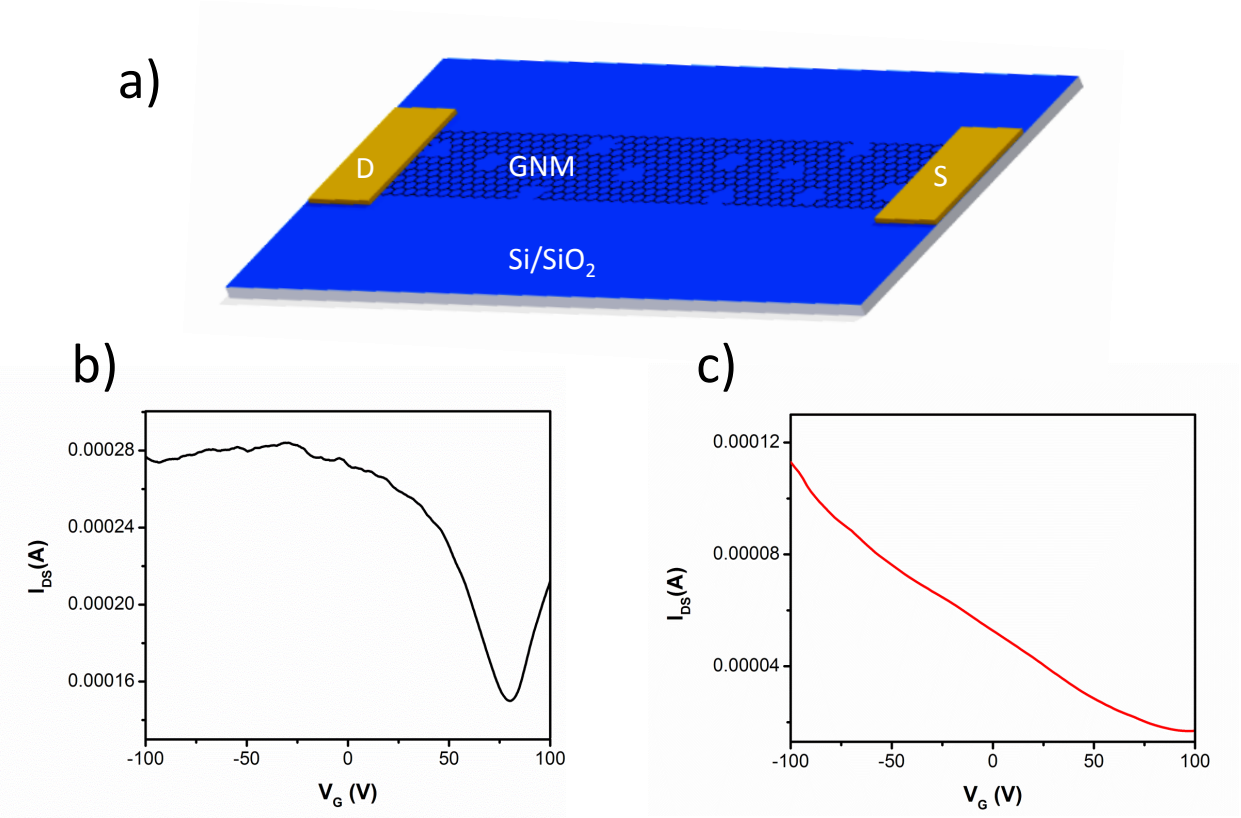


**Figure 23.** (a) Schematic illustration of a GNM FET device (b) Transfer characteristics of back-gate graphene FET device (c) Transfer characteristics of back-gate GNM FET device.

### 3.4 - Conclusion and Future Work

A simple graphene nanomesh fabrication process involving the patterning of BCP templates directly on graphene has been described. This new approach yields GNM with neck sizes of 10 nm with processes that are not damaging to underlying $Si/SiO_2$ substrates, an important factor in GNM device fabrication. Following fabrication, GNM

was studied by Raman spectroscopy. GNM FET devices prepared by photolithography demonstrate the ability to fabricate large-area semiconducting GNM devices with ON/OFF ratios greater than 6 at room temperature. Graphene synthesis by CVD and BCP lithography methods suggest a highly scalable technique towards GNM fabrication with excellent reproducibility.

Although BCP patterning directly on the surface of graphene is enticing for large-area GNM synthesis, BCP can be difficult to remove from the graphene surface due to the extremely long polymer chains and the ambiphilic nature of BCP templates used for lithography. In addition, harsh sonication treatments using strong organic solvents may damage or remove graphene from the substrate. Any remaining BCP residue on the surface of graphene may cause adverse effects to the performance of GNM devices. To address these concerns, BCP templates which allow for the complete removal of the hydrophilic block could be utilized. PS-PMMA BCP allows for the PMMA block to be removed after patterning, but previous attempts to pattern PS-PMMA templates directly on graphene have yielded unsatisfactory results[167]. Hexagonally patterned photocleavable BCPs[176] have been shown to allow the complete removal of one monomer species from the long BCP polymer chains and may by allow complete BCP removal from the graphene surface with less vigorous methods as well.

Etching of graphene by oxygen plasma has been shown to produce rough edges with no specific edge orientation. In order to open significant band gaps in graphene, channel width must be reduced to <10 nm. As channel width decreases, statistical

fluctuations due to disordered graphene edges become significant, adversely affecting the properties of graphene transistors. Smooth edges or specific graphene edge orientations are preferable to control the properties of resulting graphene transistors. GNM with smooth edges was recently obtained by nanosphere lithography on copper catalyst substrates prior to CVD growth[185]. Nanosphere lithography was used to pattern $SiO_x$ in areas protected by PS nanospheres, after CVD growth graphene grows only on exposed copper regions. Mobility measurements indicated that the mobility is three times higher in smooth edge GNM than that produced by etching graphene. However, nanosphere lithography was shown to produce GNM with neck widths of 65-75 nm, much larger than the width necessary to cause quantum confinement effects to be significant and allow semiconducting behavior.

Since the edge orientation of quantum confined graphene has significant impacts on electrical properties, an approach which controls the graphene edge-type is desirable. Anisotropic etching of graphene by hydrogen plasma was recently shown to produce selective zig-zag edge graphene[186]. Metal-assisted etching of graphene etching has been shown to remove graphene by edge selective etching, specifically copper has been shown to etch graphene along the zig-zag orientation at high temperatures in the presence of hydrogen[187,188]. Copper nanoparticles were recently shown as catalysts for the etching of graphene into GNM[189]. However, the edge orientation of graphene produced by this method was not discussed and the electrical properties of GNM materials were not examined.

A promising approach towards large-area patterning of GNM with selective edge orientation is through patterning copper nanoparticles, which can act as catalysts to etch graphene with zig-zag edges. PS-PVP BCP templates can be used to pattern regular arrays of copper nanoparticles on $SiO_2$ substrates, using a copper chloride solution to bind $Cu^{2+}$ copper ions to the PVP block. After removal of BCP by oxygen plasma, well-ordered arrays of copper nanoparticles remain on the $SiO_2$ surface. CVD-grown graphene can then be transferred on top of the copper nanoparticle array by the typical process outlined in experiments of previous studies. When heated in the presence of 10:1 Ar:$H_2$ hydrogen causes carbon absorbed on copper nanoparticles to be converted to hydrocarbon gas and carried away. Raman spectroscopy suggests that by varying the temperature of copper catalyzed graphene etching, graphene with predominantly zig-zag edges is obtained, as indicated by the splitting of the G-peak and the absence of the D-peak in GNM produced by this technique after etching at 800°C[190].

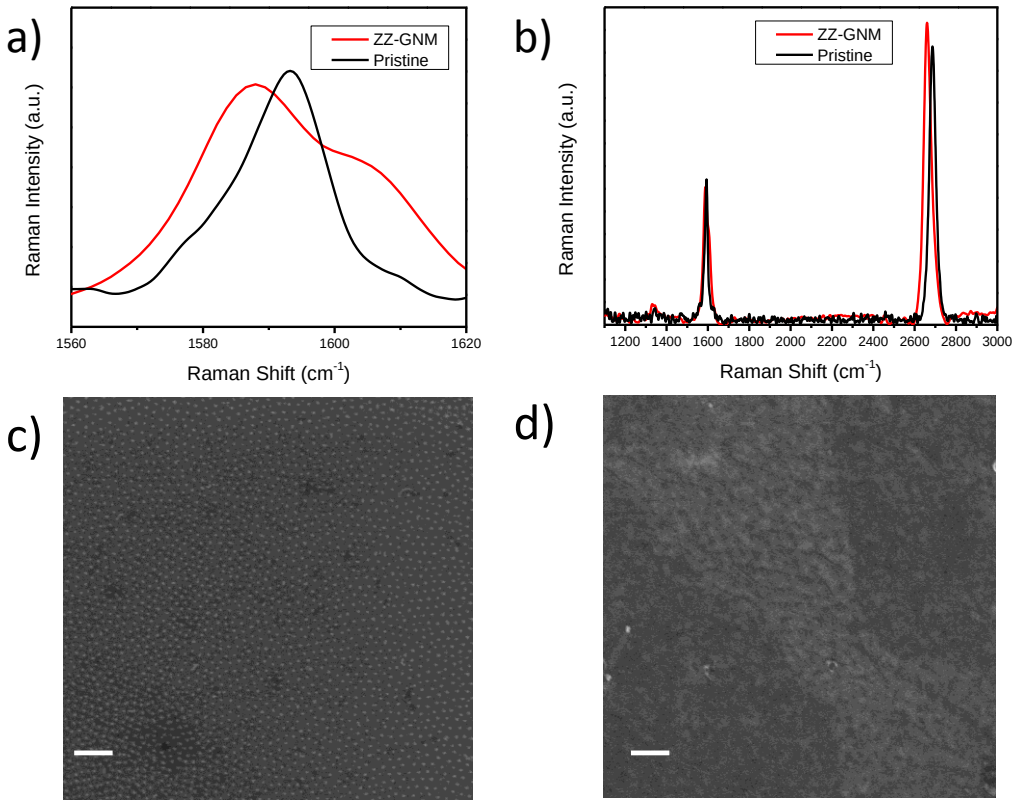


**Figure 24.** (a) Raman spectroscopy showing the shift and splitting of the G-peak, indicative of zig-zag edge graphene. (b) Raman spectroscopy showing the G/2D peak ratio is roughly conserved and the D-peak intensity is not significantly affected. (c) SEM image showing the pattern of nanoparticles used to etch the overlying graphene and (d) GNM after removing copper nanoparticles. Scale bars in (c-d) are 200 nm.

Imaging by SEM shows that the copper nanoparticles remain in a well-organized array even after annealing at 800°C. The presence of patterned nanoparticles after the annealing treatment suggests that the copper nanoparticles do not move during the

process and can only act as etching catalysts for the graphene which comes in direct contact. After GNM has been produced by the etching of copper nanoparticles, it was found that the copper nanoparticles could be etched away by a dilute mixture of $H_2O_2$:HCl (1:1) in 20 parts deionized water. The ability to etch the copper nanoparticles suggests that the copper nanoparticles have etched through the graphene layer which previously rested on top of the nanoparticles.

# Chapter 4 - Wafer-Scale Synthesis of Atomically Thin Transition Metal Dichalcogenide Layers

## 4.1 - Properties and Synthesis of Molybdenum Disulfide Thin Films

Synthesis of atomically thin $MoS_2$ layers and its derivatives with large-area uniformity is an essential step to exploit the advanced properties of $MoS_2$ for their possible applications in electronic and optoelectronic devices. In this work, a facile method for the continuous synthesis of atomically thin $MoS_2$ layers at wafer scale through thermolysis of a spin coated-ammonium tetrathiomolybdate film is reported. The thickness and surface morphology of the sheets were characterized by atomic force microscopy (AFM). The optical properties were studied by UV-vis absorption, Raman and photoluminescence spectroscopies. The compositional analysis of the layers was done by X-ray photoemission spectroscopy (XPS). The atomic structure and morphology of the grains in the polycrystalline $MoS_2$ atomic layers were examined by high-angle annular dark-field scanning transmission electron microscopy (HAADF-STEM). The electron mobilities of the sheets were evaluated using back-gate field-effect transistor configuration. The results indicate that this facile method is a promising approach to synthesize $MoS_2$ thin films at the wafer scale and can also be applied to synthesis of $WS_2$ and hybrid $MoS_2$-$WS_2$ thin layers.

Atomically thin two-dimensional (2D) transition-metal dichalcogenide (TMD) materials ($MoS_2$, $WS_2$, $MoSe_2$, $WSe_2$, $NbS_2$, $NbSe_2$, etc.) hold promise for next-

generation electronics due to enticing optical and electronic properties[115]. TMD materials exhibit a large variety of electronic behaviors such as metallic[191], semiconducting[192] and superconductivity[193]. $MoS_2$, a semiconducting TMD material, possesses an indirect band gap of ~1.3 eV in its bulk form and a direct band gap of ~1.8 eV[113] as a monolayer, allowing its realization in advanced optoelectronic devices. Moreover, large on/off current ratio ($10^8$) and abrupt switching (sub-threshold swing ~70 mV/decade) have been recently reported for monolayer $MoS_2$ transistors[194–196], suggesting promise in future electronic devices such as low power applications. In this regard, synthesis of large uniform area atomically thin $MoS_2$ films by a facile and reliable method is an essential requirement for applying these novel electronic and optical properties into future electronic and optoelectronic devices.

Recent top-down approaches such as micromechanical exfoliation[197], liquid exfoliation[198] and intercalation assisted exfoliation[199] to obtain large-area $MoS_2$ thin films have received considerable attention. However, lateral dimensions of films from these methods have been reported to be tens of micrometers, which limits their applications for large-area electronics.

Using elemental S and $MoO_3$ powder, Najmaei et al.[200] and Zande et al.[201] have recently demonstrated the bottom-up growth of centimeter scale highly crystalline $MoS_2$ films by heating in a CVD reactor. Furthermore, the sulfurization of $MoO_3$ films[202,203] has been shown to produce thin $MoS_2$ films. Although the described vapor phase synthesis

approaches show promise for future production of $MoS_2$, current production of continuous $MoS_2$ at wafer scale is still in an early stage.

### 4.2 - Thermolysis of Ammonium Tetrathiomolybdate Thin Films

Other techniques for synthesis of $MoS_2$ include the thermolysis of single liquid precursors containing Mo and S[204–206]. Synthesis of $MoS_2$ films was reported by thermolysis of the spin casted-$(NH_4)_2MoS_4$ or alkyldiammonium thiomolybdate over a decade ago[205,206], but with several nanometers in thickness and undesirable carbon residues. More recently, $MoS_2$ films have been synthesized[204] by thermolysis of dip-coated $(NH_4)_2MoS_4$ films on sapphire under sulfur pressure and transferred to $SiO_2$.

Synthesis of wafer-scale $MoS_2$ can be obtained by thermolysis of spin coated-$(NH_4)_2MoS_4$ films. Thickness of resulting $MoS_2$ films can by tuning by varying the spin coating speed and concentration of precursor solution. Additionally, thermolysis of spin coated thin films offers a method to synthesize $MoS_2$ sheets without the use of elemental sulfur powders and high temperatures. Figure 25a schematically illustrates the preparation procedure of atomically thin $MoS_2$ films.

Atomically thin $MoS_2$ films were synthesized onto 2 inch $Si/SiO_2$ wafers by thermolysis of spin coated films. Precursor solutions were prepared by dissolution of $(NH_4)_2MoS_4$ in n-methylpyrollidone (NMP). Prior to spin coating, wafers were cleaned by sonication in toluene, acetone and isopropanol, sequentially, for 45 min each. Next,

the substrates were submersed in RCA clean SC-1 (5 parts DI water, 1 part $NH_4OH$, 1 part $H_2O_2$) for 15 min. Each step is followed by a DI water rinse.

Immediately, following the cleaning procedure, the precursor films were deposited by spin coating under ambient conditions at 3000 rpm for 1 min. After spin coating deposition, the samples were moved immediately into a CVD furnace and heated to 100°C under vacuum to remove residual NMP. To complete the thermolysis, samples were annealed under $Ar/H_2$ gas flow (400/200 sccm) at 480° C for 1 h to achieve:

$$(NH_4)_2MoS_4 + H_2 \rightarrow 2NH_3 + 2H_2S + MoS_2 \qquad \textbf{(1)}$$

Subsequently, samples were annealed at 1000° C in Ar gas flow to improve crystallinity.

### 4.3 - Synthesized Molybdenum Disulfide Characterization and Device Performance

Atomic force microscopy (AFM) was used to characterize the surface morphology and thickness of $MoS_2$ thin layers. Figure 25b shows the AFM image and height profile of the $MoS_2$ film with a dewetted region, which is occasionally observed on the film. The thickness of the film is measured from the edges of the dewetted region. The inset shows that the thickness of the film is ~1.3 nm, a value consistent with the expected thickness from bilayer $MoS_2$[207]. The surface roughness value, Ra, is determined to be 0.25 nm from the height profile in Figure 25c.

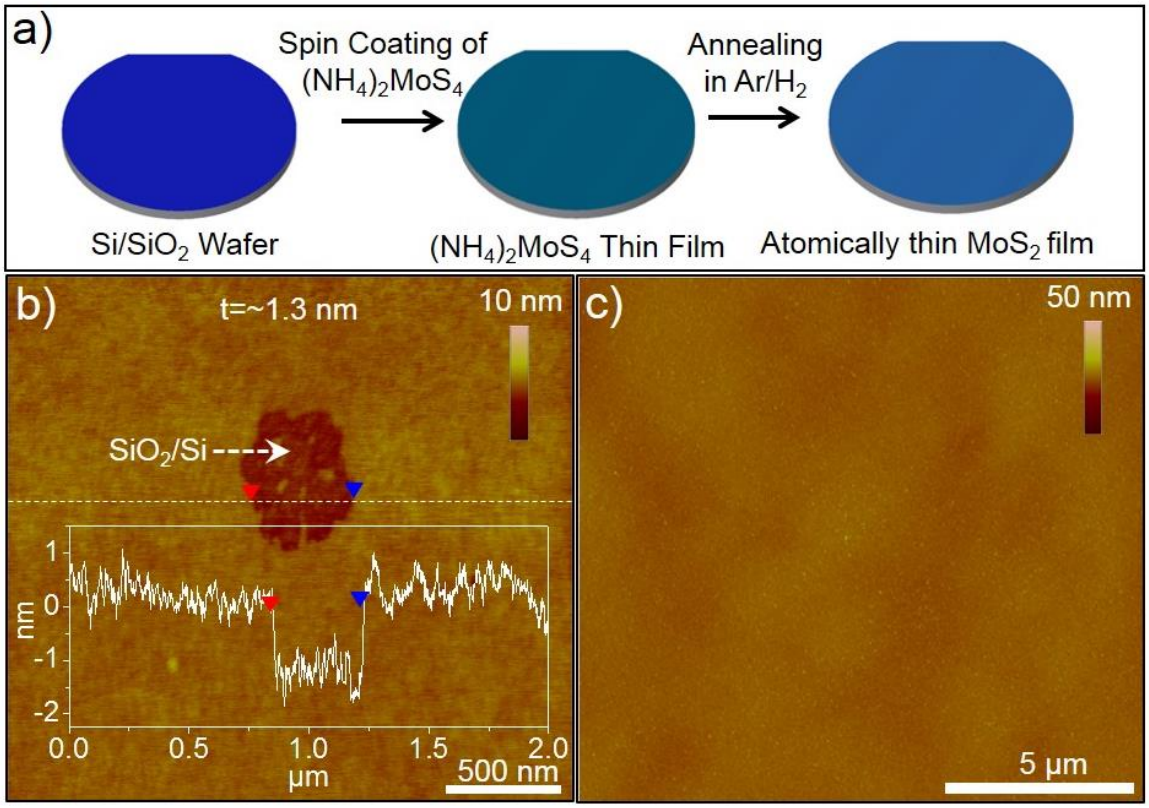


**Figure 25.** (a) Schematic representation of the preparation procedure of atomically thin $MoS_2$ films at wafer scale. AFM images and height profiles of the $MoS_2$ film in a dewetted region (b) and a continuous region (c).

For transmission electron microscopy (TEM), MoS2 sheets were coated in a protective PMMA layer by spin coating prior to the etching of $SiO_2$ in 45% KOH. Following transfer to lacey carbon TEM grids and drying, PMMA was removed by submersion in acetone. HAADF-STEM images of the $MoS_2$ film at different magnifications are shown in Figure 26. Regions of monolayers as well as double and triple layers can be identified by HAADF-STEM[208] consistent with AFM and Raman

analysis. Thicker regions, containing two or three layers, appear more intense in these images because the higher number of atoms in each atomic column leads to higher scattering of the incident electron beam into ADF detector. Figure 26c shows the characteristic hexagonal structure of $MoS_2$. Two atomic sites with distinguishable intensities can be identified at each thickness step as a result of the AB stacking of the $MoS_2$ structure, proving that the material is indeed semiconducting 2H polymorph and not metallic 1T[208]. For the monolayer 2H $MoS_2$ (Figure 26d), the higher intensity atoms were Mo, while lower intensity atoms were S as expected for HAADF-STEM imaging.

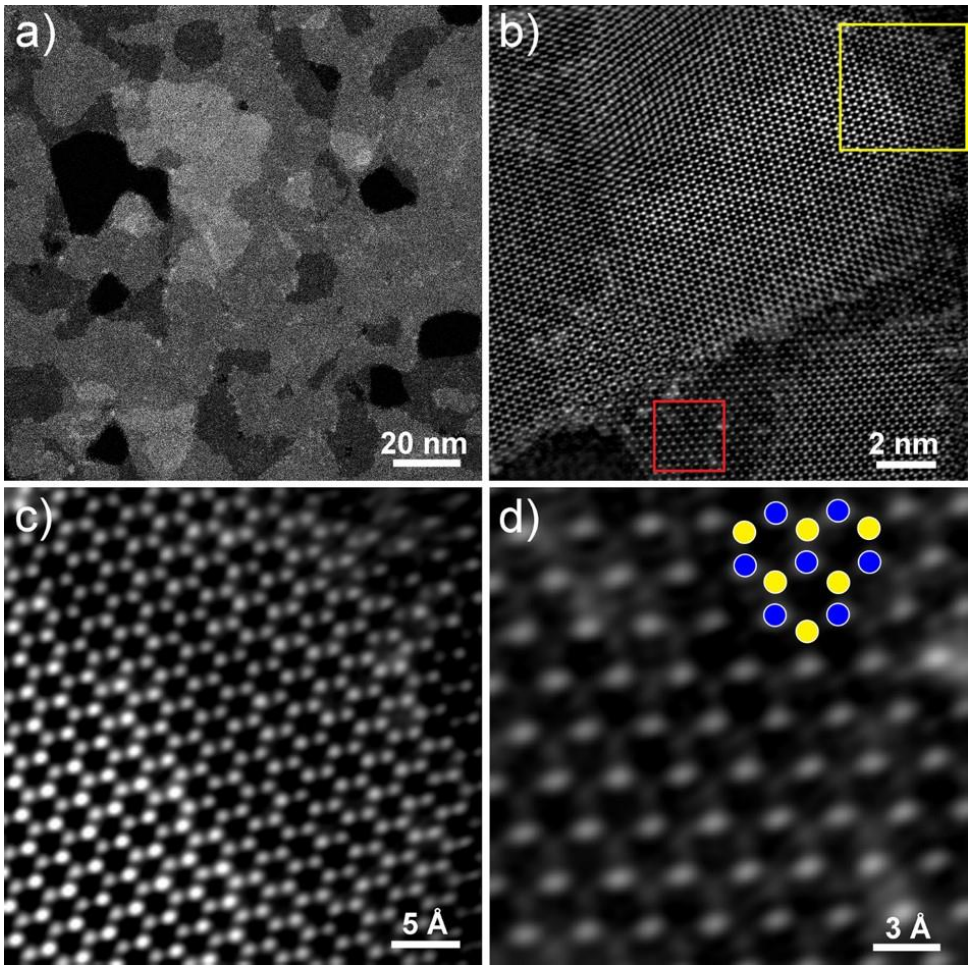


**Figure 26.** HAADF-STEM images of $MoS_2$ film: (a) low magnification; (b) intermediate magnification; (c) yellow box section of panel b showing thickness steps resulting in tri-, bi- and monolayer (left to right); (d) red box section of panel b showing monolayer $MoS_2$ with slight carbon residue (cloudy spots) with overlaid model: Mo-blue and S-yellow. All images have been filtered using 0.25 $Å^{-1}$ low-pass filter keeping Fourier peaks up to 0.9 $Å^{-1}$.

XPS was used to determine the chemical compositions and chemical states of the precursor and obtained films. Figure 27a and 27b display XPS data for Mo and S binding energies, respectively, from $MoS_2$ and $(NH_4)_2MoS_4$ films. The $(NH_4)_2MoS_4$ film exhibits two Mo 3d peaks at 232.2 and 235.5 eV, corresponding to the $3d_{3/2}$ and $3d_{5/2}$ binding energies, respectively, characteristic for the $Mo^{6+}$ state[203]. The $MoS_2$ layer also exhibits two characteristic Mo 3d peaks at 229.3 and 232.5 eV, corresponding to the $3d_{3/2}$ and $3d_{5/2}$ binding energies for the $Mo^{4+}$ state[209,210], respectively. Moreover, a shift in the binding energies of sulfur is also observed. The sulfur peak for the 2s orbital is shifted from 229.2 to 226.6 eV, while $2p_{3/2}$ and $2p_{5/2}$ peaks were shifted from 235.6 to 232.5 eV, and 232.5 to 229.3 eV, respectively, as shown in Figure 27a and 27b. Decreases in the binding energy of sulfur can be explained by the change of oxidation state of Mo from $Mo^{6+}$ to $Mo^{4+}$, which causes a decrease in the bond strength between molybdenum and sulfur. The results confirm the change of oxidation state of Mo from $Mo^{6+}$ to $Mo^{4+}$ and the complete transition from $(NH_4)_2MoS_4$ to $MoS_2$.

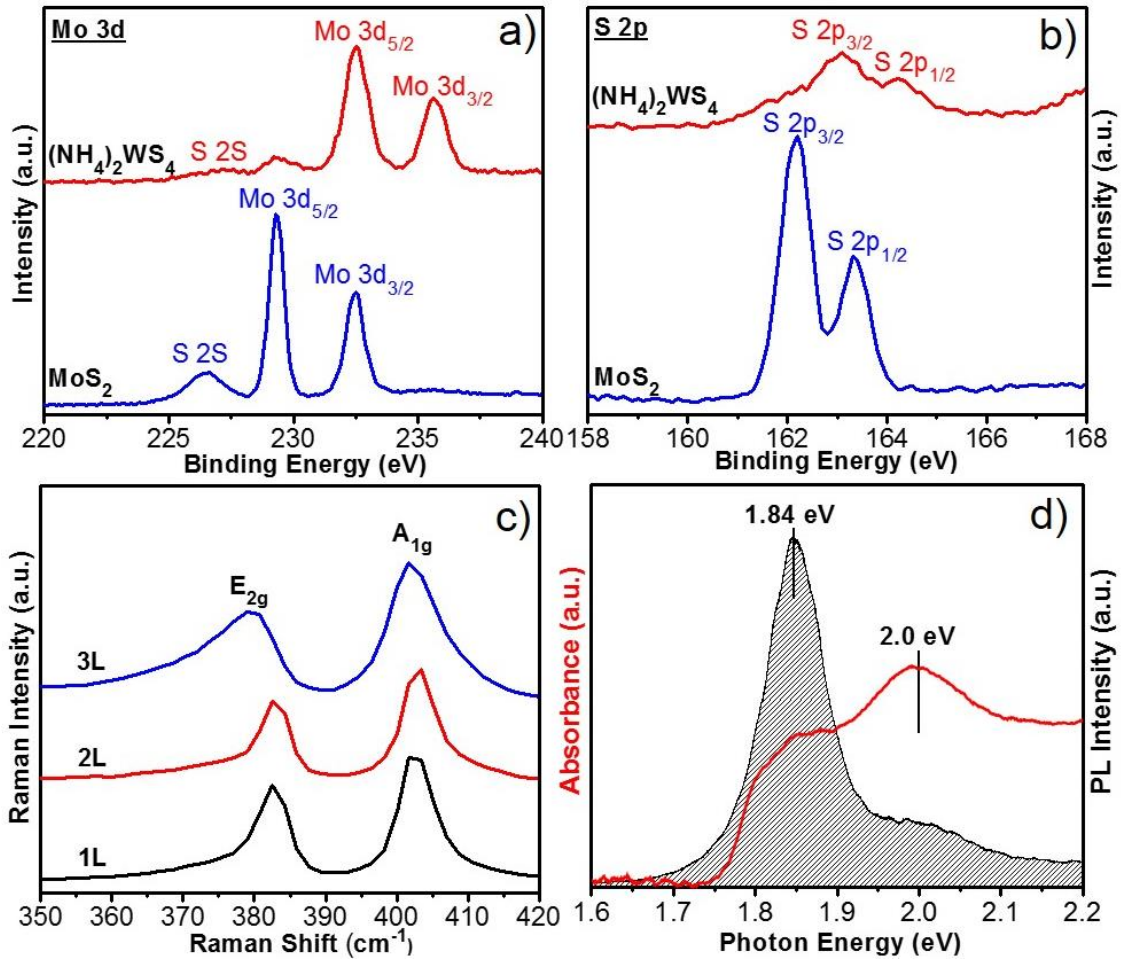


**Figure 27.** XPS data of (a) Mo and (b) S binding energies from the $MoS_2$ and $(NH_4)_2MoS_4$ films. (c) Raman spectra from 1, 2 and 3 $MoS_2$ layers on the film (d) PL and absorption spectra from the film.

Raman spectroscopy is a powerful nondestructive characterization tool which can be used to reveal the crystallinity and thickness of atomically thin materials. Figure 27c shows the Raman spectrum from 1, 2 and 3 layers on the $MoS_2$ film at room temperature. The spectrum reveals two characteristic Raman modes of $MoS_2$, $E_{2g}$ and $A_{1g}$. The

frequency difference between $E_{2g}$ and $A_{1g}$ phonons has been shown as an indicator of the number of layers in $MoS_2$[211,212]**.** The observed frequency difference between the $E_{2g}$ and $A_{1g}$ peaks was 19.3 $cm^{-1}$, corresponding to monolayer $MoS_2$[113]. Other areas of the $MoS_2$ film show a red shift of $E_{2g}$ peak and blue shift of $A_{1g}$ peak, causing increasing peak spacing between $E_{2g}$ and $A_{1g}$ modes as the number of layers in the $MoS_2$ thin film increases, indicating the presence of two and three layer regions.

To further investigate the quality of $MoS_2$ films, photoluminescence (PL) and absorption spectroscopy measurements were performed at room temperature. The PL spectrum in Figure 27d reveals an intense peak at 1.84 eV, confirming the presence of the direct band gap in atomically thin $MoS_2$[213,214]. Figure 27d also shows the absorption spectra of the $MoS_2$ film. The spectra reveals two absorption peaks at 1.84 eV and 2.0 eV, corresponding to the A1 and B1 direct excitonic transitions at the Brillouin zone K point[215].

To evaluate the electrical transport properties of the $MoS_2$ film, back-gate field-effect transistors (FETs) were fabricated on the top of the $MoS_2$ layers on $SiO_2$/Si with Ti/Au (10/80 nm) contacts. The corresponding transfer and output plots are shown in Figure 28. The field-effect mobility was extracted using the equation $\mu=(\Delta Id/\Delta Vg)/(\varepsilon VdW/L_{ox}L)$[192], where $L_{ox}$ is oxidation thickness (300 nm), L is the length of the channel, W is the channel width, ε is the gate dielectric ($\varepsilon_{SiO2}$ = 3.9), and ($\Delta Id/\Delta Vg$) is the slope calculated from Figure 28a. The electron mobility of $MoS_2$ from this growth method was calculated to be ~ 0.1 $cm^2V^{-1}s^{-1}$, which is in agreement of earlier

reports on the characterization of $MoS_2$ layers synthesized by the CVD method[113,216]. ON/OFF ratio for the device shown (ON/OFF = 338) may be increased for $V_g > 100$ V.

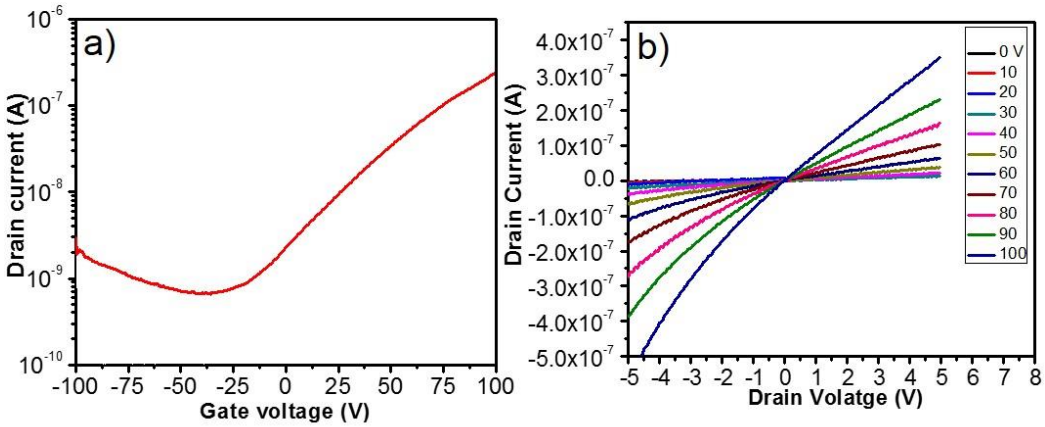


**Figure 28.** (a) Plot of drain current vs. gate voltage shows electron transport using Ti/Au contacts, where $V_{DS} = 2$ V. ON/OFF ratio for this device is ~3 x $10^2$. (b) Drain current vs. drain-source voltage characteristics.

To demonstrate the versatility of the method described above, the synthesis of $WS_2$ from ammonium tetrathiotungstate, $(NH_4)_2WS_4$, was performed in a similar manner to that of $MoS_2$. The Raman spectra reveals two main characteristics peaks, $E_{2g}$ and $A_{1g}$, of $WS_2$[217], shown by Figure 29a. PL spectrum shows an excitation centered at 2.0 eV (Figure 29b)[218]. Both Raman and PL spectroscopy results confirm the thin film nature of the grown films by this technique[217,219]. Hybrid $MoS_2$-$WS_2$ materials can be also synthesized with this approach by simply combining precursors $(NH_4)_2MoS_4$ and

$(NH_4)_2WS_4$ in solution prior to spin coating, as confirmed by the Raman spectra in Figure 29c[220,221]. After thermolysis of the two precursor film, an alloy in the form of $Mo_xW_{2-x}S_2$ can be achieved, where x denotes the proportion of Mo and W in the resulting film. PL of the hybrid $MoS_2$-$WS_2$ film produced by equal amounts of $(NH_4)_2MoS_4$ and $(NH_4)_2WS_4$ shows an excitation at 1.85 eV, consistent with previous reports of $Mo_xW_{2-x}S_2$ films[214]. It is straightforward to envision how this process can be utilized to achieve homogenous alloys and doping of TMDs[222].

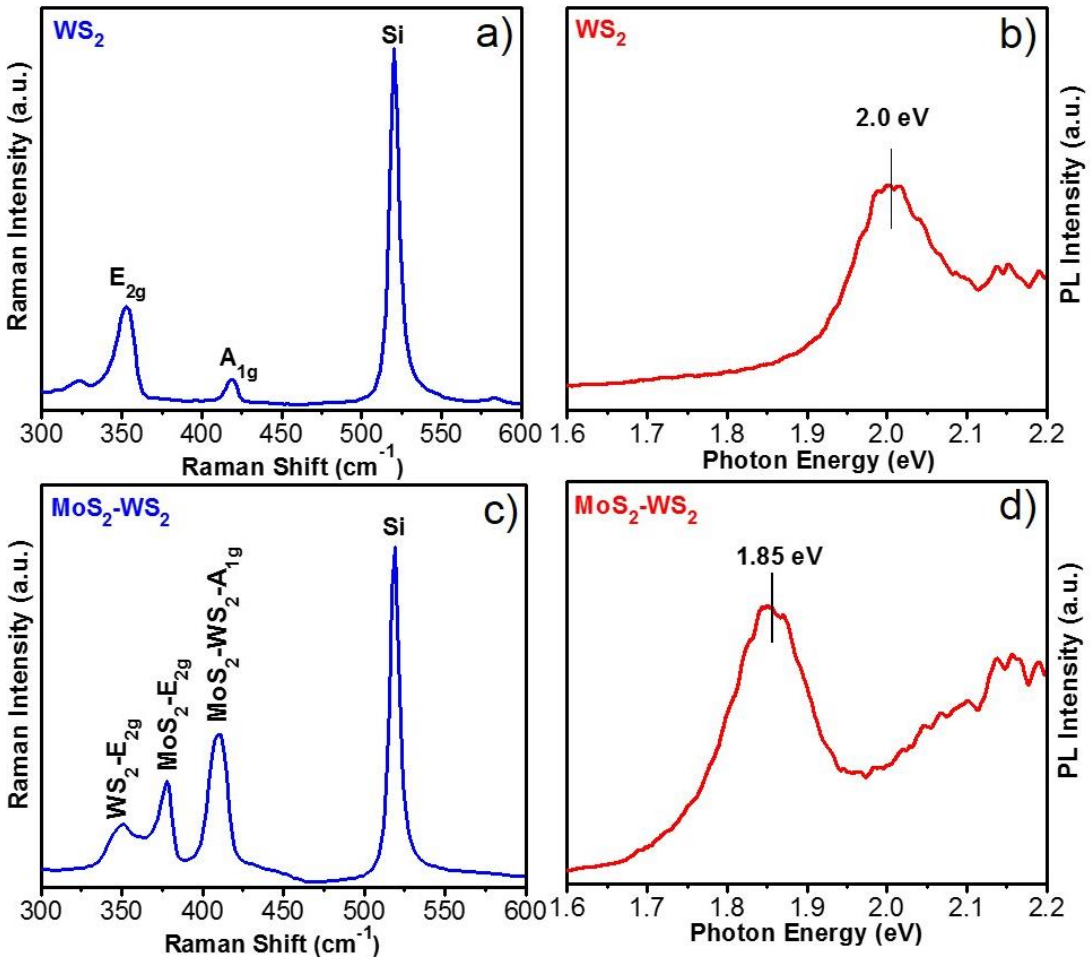


**Figure 29.** (a,c) Raman and (b,d) PL spectra of $WS_2$ and $Mo_xW_{2-x}S_2$ film.

### 4.4 - Conclusion and Future Work

In summary, the synthesis of $MoS_2$ layers by the thermolysis of spin coated thin films has been demonstrated on the wafer scale. Samples may be prepared down to monolayer thickness, as revealed by TEM analysis. Back-gate FET devices were fabricated directly on the $Si/SiO_2$ substrate used for growth and show mobilities of 0.1

$cm^2V^{-1}s^{-1}$. This approach may be applied to numerous substrates and suggests a promising route towards the production of other TMD materials, alloyed or electronically doped TMD materials. Thin $WS_2$ and hybrid $MoS_2$-$WS_2$ films have been produced successfully with this method, as confirmed by Raman spectroscopy, offering synthesis of TMDs with tunable bandgap for future electronics applications. This process provides smooth, uniform, layer-controlled synthesis by a facile method which can exclude the use of elemental sulfur, showing promise in TMD synthesis for future electronics applications.

Large-area synthesis of monolayer $MoS_2$ is an exciting step towards future $MoS_2$ semiconducting devices. On the other hand, transport characteristics of CVD synthesized $MoS_2$ are inferior to that of exfoliated $MoS_2$. Similarly to graphene, CVD produced $MoS_2$ is hindered by scattering events at $MoS_2$ grains. Furthermore, when separate $MoS_2$ grains are expanding during a CVD growth process come together, grains merge to form various usual atomic rings which adversely affect the electronic states of the material[200,201]. Future work is needed to produce methods which can expand dimensions single crystal domains in CVD grown $MoS_2$.

Electronic doping of TMD materials has not yet been explored in depth by researchers. Thermolysis of solution-processed precursors may offer the ability to precisely control the doping of TMD materials by the mixing of multiple precursors in solution prior to deposition on the substrate of choice. For instance, a dilute solution of $(NH_4)_3VS_4$ may be mixed with $(NH_4)_2MoS_4$ to form a desired level of p-type doping by

tuning the molecular ratio of the starting solution. However, similar TMD precursors are commercially limited and experimental details of the preparation procedures are not trivial. Incorporation of sulfur into compounds involves the replacement of oxygen in materials such as $NH_4VO_3$ by continual flow of $H_2S$ or by addition of $(NH_4)SH$. Other dichalcogenides species may be incorporated by similar methods but these methods have not been well studied at this time. Moreover, precursors such as $(NH_4)_3VS_4$ are sensitive to oxidization in powder form and choice of solvents are consequently limited. Therefore, thermolysis of precursors deposited from solution may be limited for the synthesis of TMD materials.

## References


(1) Geim, A. K.; Novoselov, K. S. The Rise of Graphene. Nature Materials 2007, 6, 183–191.

(2) Danneau, R.; Wu, F.; Craciun, M.; Russo, S.; Tomi, M.; Salmilehto, J.; Morpurgo, A.; Hakonen, P. Shot Noise in Ballistic Graphene. Physical Review Letters 2008, 100.

(3) Balandin, A. A.; Ghosh, S.; Bao, W.; Calizo, I.; Teweldebrhan, D.; Miao, F.; Lau, C. N. Superior Thermal Conductivity of Single-Layer Graphene. Nano Letters 2008, 8, 902–907.

(4) Nair, R. R.; Blake, P.; Grigorenko, A. N.; Novoselov, K. S.; Booth, T. J.; Stauber, T.; Peres, N. M. R.; Geim, A. K. Fine Structure Constant Defines Visual Transparency of Graphene. Science 2008, 320, 1308–1308.

(5) Lee, C.; Wei, X.; Kysar, J. W.; Hone, J. Measurement of the Elastic Properties and Intrinsic Strength of Monolayer Graphene. Science 2008, 321, 385–388.

(6) Wallace, P. The Band Theory of Graphite. Physical Review 1947, 71, 622–634.

(7) DiVincenzo, D. P.; Mele, E. J. Self-Consistent Effective-Mass Theory for Intralayer Screening in Graphite Intercalation Compounds. Physical Review B 1984, 29, 1685–1694.

(8) Mouras, S.; Hamm, A.; Djurado, D.; Cousseins, J. C. Synthesis of First Stage Graphite Intercalation Compounds with Fluorides. Gauthier-Villars: Paris, France 1987, 24, 572–582.

(9) Novoselov, K. S. Electric Field Effect in Atomically Thin Carbon Films. Science 2004, 306, 666–669.

(10) Fasolino, A.; Los, J. H.; Katsnelson, M. I. Intrinsic Ripples in Graphene. Nature Materials 2007, 6, 858–861.

(11) Kroto, H. W.; Heath, J. R.; O'Brien, S. C.; Curl, R. F.; Smalley, R. E. $C_{60}$: Buckminsterfullerene. Nature 1985, 318, 162–163.

(12) Monthioux, M.; Kuznetsov, V. L. Who should be given the credit for the discovery of carbon nanotubes? Carbon 2006, 44, 1621–1623.

(13) Mintmire, J. W.; Dunlap, B. I.; White, C. T. Are Fullerene Tubules Metallic? Physical Review Letters 1992, 68, 631–634.

(14) Wang, X.; Li, Q.; Xie, J.; Jin, Z.; Wang, J.; Li, Y.; Jiang, K.; Fan, S. Fabrication of Ultralong and Electrically Uniform Single-Walled Carbon Nanotubes on Clean Substrates. Nano Letters 2009, 9, 3137–3141.

(15) Hamada, N.; Sawada, S.; Oshiyama, A. New One-Dimensional Conductors: Graphitic Microtubules. Physical Review Letters 1992, 68, 1579–1581.

(16) Saito, R.; Fujita, M.; Dresselhaus, G.; Dresselhaus, M. S. Electronic Structure of Chiral Graphene Tubules. Applied Physics Letters 1992, 60, 2204.

(17) Saito, R.; Fujita, M.; Dresselhaus, G.; Dresselhaus, M. Electronic Structure of Graphene Tubules Based on $C_{60}$. Physical Review B 1992, 46, 1804–1811.

(18) "The Nobel Prize in Physics 2010". Nobelprize.org. Nobel Media AB 2014. Web. 4 Nov 2014. <http://www.nobelprize.org/nobel_prizes/physics/laureates/2010/>.

(19) Zhan, D.; Yan, J.; Lai, L.; Ni, Z.; Liu, L.; Shen, Z. Engineering the Electronic Structure of Graphene. Advanced Materials 2012, 24, 4055–4069.

(20) McCann, E.; Fal'ko, V. Landau-Level Degeneracy and Quantum Hall Effect in a Graphite Bilayer. Physical Review Letters 2006, 96.

(21) Zhang, Y.; Tan, Y.-W.; Stormer, H. L.; Kim, P. Experimental Observation of the Quantum Hall Effect and Berry's Phase in Graphene. Nature 2005, 438, 201–204.

(22) Lang, B. A LEED Study of the Deposition of Carbon on Platinum Crystal Surfaces. Surface Science 1975, 53, 317–329.

(23) Viculis, L. M. A Chemical Route to Carbon Nanoscrolls. Science 2003, 299, 1361–1361.

(24) Novoselov, K. S.; Jiang, D.; Schedin, F.; Booth, T. J.; Khotkevich, V. V.; Morozov, S. V.; Geim, A. K. Two-Dimensional Atomic Crystals. Proceedings of the National Academy of Sciences 2005, 102, 10451–10453.

(25) Choi, W.; Lahiri, I.; Seelaboyina, R.; Kang, Y. S. Synthesis of Graphene and Its Applications: A Review. Critical Reviews in Solid State and Materials Sciences 2010, 35, 52–71.

(26) Calizo, I.; Balandin, A. A.; Bao, W.; Miao, F.; Lau, C. N. Temperature Dependence of the Raman Spectra of Graphene and Graphene Multilayers. Nano Letters 2007, 7, 2645–2649.

(27) Pisana, S.; Lazzeri, M.; Casiraghi, C.; Novoselov, K. S.; Geim, A. K.; Ferrari, A. C.; Mauri, F. Breakdown of the Adiabatic Born–Oppenheimer Approximation in Graphene. Nature Materials 2007, 6, 198–201.

(28) Novoselov, K. S.; Fal′ko, V. I.; Colombo, L.; Gellert, P. R.; Schwab, M. G.; Kim, K. A Roadmap for Graphene. Nature 2012, 490, 192–200.

(29) Kretinin, A. V.; Cao, Y.; Tu, J. S.; Yu, G. L.; Jalil, R.; Novoselov, K. S.; Haigh, S. J.; Gholinia, A.; Mishchenko, A.; Lozada, M.; et al. Electronic Properties of Graphene Encapsulated with Different Two-Dimensional Atomic Crystals. Nano Letters 2014, 14, 3270–3276.

(30) Dresselhaus, M. S.; Dresselhaus, G.; Saito, R.; Jorio, A. Chapter 4 Raman Spectroscopy of Carbon Nanotubes. In Contemporary Concepts of Condensed Matter Science; Elsevier, 2008; Vol. 3, pp. 83–108.

(31) Huang, M.; Yan, H.; Chen, C.; Song, D.; Heinz, T. F.; Hone, J. Phonon Softening and Crystallographic Orientation of Strained Graphene Studied by Raman Spectroscopy. Proceedings of the National Academy of Sciences 2009, 106, 7304–7308.

(32) Calizo, I.; Bejenari, I.; Rahman, M.; Liu, G.; Balandin, A. A. Ultraviolet Raman Microscopy of Single and Multilayer Graphene. Journal of Applied Physics 2009, 106, 043509.

(33) Filintoglou, K.; Papadopoulos, N.; Arvanitidis, J.; Christofilos, D.; Frank, O.; Kalbac, M.; Parthenios, J.; Kalosakas, G.; Galiotis, C.; Papagelis, K. Raman Spectroscopy of Graphene at High Pressure: Effects of the Substrate and the Pressure Transmitting Media. Physical Review B 2013, 88.

(34) Ferrari, A. C. Raman Spectroscopy of Graphene and Graphite: Disorder, Electron–phonon Coupling, Doping and Nonadiabatic Effects. Solid State Communications 2007, 143, 47–57.

(35) Jorio, A.; Saito, R.; Dresselhaus, G.; Dresselhaus, M. S. (2010) Raman Spectroscopy in Graphene Related Systems. John Wiley & Sons.

(36) Graf, D.; Molitor, F.; Ensslin, K.; Stampfer, C.; Jungen, A.; Hierold, C.; Wirtz, L. Spatially Resolved Raman Spectroscopy of Single- and Few-Layer Graphene. Nano Letters 2007, 7, 238–242.

(37) Stankovich, S.; Piner, R. D.; Nguyen, S. T.; Ruoff, R. S. Synthesis and Exfoliation of Isocyanate-Treated Graphene Oxide Nanoplatelets. Carbon 2006, 44, 3342–3347.

(38) Stankovich, S.; Piner, R. D.; Chen, X.; Wu, N.; Nguyen, S. T.; Ruoff, R. S. Stable Aqueous Dispersions of Graphitic Nanoplatelets via the Reduction of Exfoliated Graphite Oxide in the Presence of Poly(sodium 4-Styrenesulfonate). Journal of Materials Chemistry 2006, 16, 155.

(39) Hernandez, Y.; Nicolosi, V.; Lotya, M.; Blighe, F. M.; Sun, Z.; De, S.; McGovern, I. T.; Holland, B.; Byrne, M.; Gun'Ko, Y. K.; et al. High-Yield Production of Graphene by Liquid-Phase Exfoliation of Graphite. Nature Nanotechnology 2008, 3, 563–568.

(40) Lotya, M.; Hernandez, Y.; King, P. J.; Smith, R. J.; Nicolosi, V.; Karlsson, L. S.; Blighe, F. M.; De, S.; Wang, Z.; McGovern, I. T.; et al. Liquid Phase Production of Graphene by Exfoliation of Graphite in Surfactant/Water Solutions. Journal of the American Chemical Society 2009, 131, 3611–3620.

(41) Nuvoli, D.; Valentini, L.; Alzari, V.; Scognamillo, S.; Bon, S. B.; Piccinini, M.; Illescas, J.; Mariani, A. High Concentration Few-Layer Graphene Sheets Obtained by Liquid Phase Exfoliation of Graphite in Ionic Liquid. Journal of Materials Chemistry 2011, 21, 3428.

(42) Wu, X.; Li, X.; Song, Z.; Berger, C.; de Heer, W. A. Weak Antilocalization in Epitaxial Graphene: Evidence for Chiral Electrons. Physical Review Letters 2007, 98.

(43) Sadowski, M. L.; Martinez, G.; Potemski, M. Landau Level Spectroscopy of Ultrathin Graphite Layers. Physical Review Letters 2006, 97.

(44) Hass, J.; Varchon, F.; Millán-Otoya, J.; Sprinkle, M.; Sharma, N.; de Heer, W.; Berger, C.; First, P.; Magaud, L.; Conrad, E. Why Multilayer Graphene on 4H-SiC($000\bar{1}$) Behaves Like a Single Sheet of Graphene. Physical Review Letters 2008, 100.

(45) Bostwick, A.; Ohta, T.; McChesney, J. L.; Emtsev, K. V.; Seyller, T.; Horn, K.; Rotenberg, E. Symmetry Breaking in Few Layer Graphene Films. New Journal of Physics 2007, 9, 385–385.

(46) Tzalenchuk, A.; Lara-Avila, S.; Kalaboukhov, A.; Paolillo, S.; Syväjärvi, M.; Yakimova, R.; Kazakova, O.; Janssen, T. J. B. M.; Fal'ko, V.; Kubatkin, S. Towards a Quantum Resistance Standard Based on Epitaxial Graphene. Nature Nanotechnology 2010, 5, 186–189.

(47) Zhou, S. Y.; Gweon, G.-H.; Graf, J.; Fedorov, A. V.; Spataru, C. D.; Diehl, R. D.; Kopelevich, Y.; Lee, D.-H.; Louie, S. G.; Lanzara, A. First Direct Observation of Dirac Fermions in Graphite. Nature Physics 2006, 2, 595–599.

(48) Paton, K. R.; Varrla, E.; Backes, C.; Smith, R. J.; Khan, U.; O'Neill, A.; Boland, C.; Lotya, M.; Istrate, O. M.; King, P.; et al. Scalable Production of Large Quantities of Defect-Free Few-Layer Graphene by Shear Exfoliation in Liquids. Nature Materials 2014, 13, 624–630.

(49) Jobst, J.; Waldmann, D.; Speck, F.; Hirner, R.; Maude, D. K.; Seyller, T.; Weber, H. B. Quantum Oscillations and Quantum Hall Effect in Epitaxial Graphene. Physical Review B 2010, 81.

(50) Shen, T.; Gu, J. J.; Xu, M.; Wu, Y. Q.; Bolen, M. L.; Capano, M. A.; Engel, L. W.; Ye, P. D. Observation of Quantum-Hall Effect in Gated Epitaxial Graphene Grown on SiC (0001). Applied Physics Letters 2009, 95, 172105.

(51) Wu, X.; Hu, Y.; Ruan, M.; Madiomanana, N. K.; Hankinson, J.; Sprinkle, M.; Berger, C.; de Heer, W. A. Half Integer Quantum Hall Effect in High Mobility Single Layer Epitaxial Graphene. Applied Physics Letters 2009, 95, 223108.

(52) Alexander-Webber, J. A.; Baker, A. M. R.; Janssen, T. J. B. M.; Tzalenchuk, A.; Lara-Avila, S.; Kubatkin, S.; Yakimova, R.; Piot, B. A.; Maude, D. K.; Nicholas, R. J. Phase Space for the Breakdown of the Quantum Hall Effect in Epitaxial Graphene. Physical Review Letters 2013, 111.

(53) Berger, C. Electronic Confinement and Coherence in Patterned Epitaxial Graphene. Science 2006, 312, 1191–1196.

(54) Hass, J.; de Heer, W. A.; Conrad, E. H. The Growth and Morphology of Epitaxial Multilayer Graphene. Journal of Physics: Condensed Matter 2008, 20, 323202.

(55) Van Bommel, A. J.; Crombeen, J. E.; Van Tooren, A. LEED and Auger Electron Observations of the SiC(0001) Surface. Surface Science 1975, 48, 463–472.

(56) Juang, Z.-Y.; Wu, C.-Y.; Lo, C.-W.; Chen, W.-Y.; Huang, C.-F.; Hwang, J.-C.; Chen, F.-R.; Leou, K.-C.; Tsai, C.-H. Synthesis of Graphene on Silicon Carbide Substrates at Low Temperature. Carbon 2009, 47, 2026–2031.

(57) Emtsev, K. V.; Bostwick, A.; Horn, K.; Jobst, J.; Kellogg, G. L.; Ley, L.; McChesney, J. L.; Ohta, T.; Reshanov, S. A.; Röhrl, J.; et al. Towards Wafer-Size Graphene Layers by Atmospheric Pressure Graphitization of Silicon Carbide. Nature Materials 2009, 8, 203–207.

(58) Avouris, P.; Xia, F. Graphene Applications in Electronics and Photonics. MRS Bulletin 2012, 37, 1225–1234.

(59) Somani, P. R.; Somani, S. P.; Umeno, M. Planer Nano-Graphenes from Camphor by CVD. Chemical Physics Letters 2006, 430, 56–59.

(60) Mattevi, C.; Kim, H.; Chhowalla, M. A Review of Chemical Vapour Deposition of Graphene on Copper. Journal of Materials Chemistry 2011, 21, 3324.

(61) Obraztsov, A. N.; Obraztsova, E. A.; Tyurnina, A. V.; Zolotukhin, A. A. Chemical Vapor Deposition of Thin Graphite Films of Nanometer Thickness. Carbon 2007, 45, 2017–2021.

(62) Yu, Q.; Lian, J.; Siriponglert, S.; Li, H.; Chen, Y. P.; Pei, S.-S. Graphene Segregated on Ni Surfaces and Transferred to Insulators. Applied Physics Letters 2008, 93, 113103.

(63) Kim, K. S.; Zhao, Y.; Jang, H.; Lee, S. Y.; Kim, J. M.; Kim, K. S.; Ahn, J.-H.; Kim, P.; Choi, J.-Y.; Hong, B. H. Large-Scale Pattern Growth of Graphene Films for Stretchable Transparent Electrodes. Nature 2009, 457, 706–710.

(64) Reina, A.; Jia, X.; Ho, J.; Nezich, D.; Son, H.; Bulovic, V.; Dresselhaus, M. S.; Kong, J. Large Area, Few-Layer Graphene Films on Arbitrary Substrates by Chemical Vapor Deposition. Nano Letters 2009, 9, 30–35.

(65) Gong, Y.; Zhang, X.; Liu, G.; Wu, L.; Geng, X.; Long, M.; Cao, X.; Guo, Y.; Li, W.; Xu, J.; et al. Layer-Controlled and Wafer-Scale Synthesis of Uniform and High-Quality Graphene Films on a Polycrystalline Nickel Catalyst. Advanced Functional Materials 2012, 22, 3153–3159.

(66) Tuinstra, F. Raman Spectrum of Graphite. The Journal of Chemical Physics 1970, 53, 1126.

(67) McLellan, R. B. The Solubility of Carbon in Solid Gold, Copper, and Silver. Scripta Metallurgica 1969, 3, 389–391.

(68) Li, X.; Cai, W.; An, J.; Kim, S.; Nah, J.; Yang, D.; Piner, R.; Velamakanni, A.; Jung, I.; Tutuc, E.; et al. Large-Area Synthesis of High-Quality and Uniform Graphene Films on Copper Foils. Science 2009, 324, 1312–1314.

(69) Calado, V. E.; Zhu, S.-E.; Goswami, S.; Xu, Q.; Watanabe, K.; Taniguchi, T.; Janssen, G. C. A. M.; Vandersypen, L. M. K. Ballistic Transport in Graphene Grown by Chemical Vapor Deposition. Applied Physics Letters 2014, 104, 023103.

(70) Hao, Y.; Bharathi, M. S.; Wang, L.; Liu, Y.; Chen, H.; Nie, S.; Wang, X.; Chou, H.; Tan, C.; Fallahazad, B.; et al. The Role of Surface Oxygen in the Growth of Large Single-Crystal Graphene on Copper. Science 2013, 342, 720–723.

(71) Chen, S.; Ji, H.; Chou, H.; Li, Q.; Li, H.; Suk, J. W.; Piner, R.; Liao, L.; Cai, W.; Ruoff, R. S. Millimeter-Size Single-Crystal Graphene by Suppressing Evaporative Loss of Cu During Low Pressure Chemical Vapor Deposition. Advanced Materials 2013, 25, 2062–2065.

(72) Song, L.; Ci, L.; Gao, W.; Ajayan, P. M. Transfer Printing of Graphene Using Gold Film. ACS Nano 2009, 3, 1353–1356.

(73) Reina, A.; Son, H.; Jiao, L.; Fan, B.; Dresselhaus, M. S.; Liu, Z.; Kong, J. Transferring and Identification of Single- and Few-Layer Graphene on Arbitrary Substrates. The Journal of Physical Chemistry C 2008, 112, 17741–17744.

(74) Su, C.-Y.; Lu, A.-Y.; Wu, C.-Y.; Li, Y.-T.; Liu, K.-K.; Zhang, W.; Lin, S.-Y.; Juang, Z.-Y.; Zhong, Y.-L.; Chen, F.-R.; et al. Direct Formation of Wafer Scale Graphene Thin Layers on Insulating Substrates by Chemical Vapor Deposition. Nano Letters 2011, 11, 3612–3616.

(75) Peng, Z.; Yan, Z.; Sun, Z.; Tour, J. M. Direct Growth of Bilayer Graphene on $SiO_2$ Substrates by Carbon Diffusion through Nickel. ACS Nano 2011, 5, 8241–8247.

(76) Gao, L.; Ni, G.-X.; Liu, Y.; Liu, B.; Castro Neto, A. H.; Loh, K. P. Face-to-Face Transfer of Wafer-Scale Graphene Films. Nature 2013, 505, 190–194.

(77) Bae, S.; Kim, H.; Lee, Y.; Xu, X.; Park, J.-S.; Zheng, Y.; Balakrishnan, J.; Lei, T.; Ri Kim, H.; Song, Y. I.; et al. Roll-to-Roll Production of 30-Inch Graphene Films for Transparent Electrodes. Nature Nanotechnology 2010, 5, 574–578.

(78) Kyle, J. R.; Ozkan, C. S.; Ozkan, M. Industrial Graphene Metrology. Nanoscale 2012, 4, 3807.

(79) Kyle, J. R.; Guvenc, A.; Wang, W.; Ghazinejad, M.; Lin, J.; Guo, S.; Ozkan, C. S.; Ozkan, M. Centimeter-Scale High-Resolution Metrology of Entire CVD-Grown Graphene Sheets. Small 2011, 7, 2599–2606.

(80) Pirkle, A.; Chan, J.; Venugopal, A.; Hinojos, D.; Magnuson, C. W.; McDonnell, S.; Colombo, L.; Vogel, E. M.; Ruoff, R. S.; Wallace, R. M. The Effect of Chemical Residues on the Physical and Electrical Properties of Chemical Vapor Deposited Graphene Transferred to $SiO_2$. Applied Physics Letters 2011, 99, 122108.

(81) Adam, S.; Hwang, E. H.; Galitski, V. M.; Das Sarma, S. A Self-Consistent Theory for Graphene Transport. Proceedings of the National Academy of Sciences 2007, 104, 18392–18397.

(82) Ishigami, M.; Chen, J. H.; Cullen, W. G.; Fuhrer, M. S.; Williams, E. D. Atomic Structure of Graphene on $SiO_2$. Nano Letters 2007, 7, 1643–1648.

(83) Kedzierski, J.; Pei-Lan Hsu; Reina, A.; Jing Kong; Healey, P.; Wyatt, P.; Keast, C. Graphene-on-Insulator Transistors Made Using C on Ni Chemical-Vapor Deposition. IEEE Electron Device Letters 2009, 30, 745–747.

(84) "The Nobel Prize in Physics 1956". Nobelprize.org. Nobel Media AB 2014. Web. 5 Nov 2014. <http://www.nobelprize.org/nobel_prizes/physics/laureates/1956/>.

(85) Moore, G. E. Cramming more components onto integrated circuits. Proceedings of the IEEE 1998, 86, 82–85.

(86) Anderson, R. G. How Well Do Wages Follow Productivity Growth? National Economic Trends, Federal Reserve Bank of St. Louis.

(87) Borkar, S.; Chien, A. A. The Future of Microprocessors. Communications of the ACM 2011, 54, 67.

(88) Schwierz, F. Graphene Transistors. Nature Nanotechnology 2010, 5, 487–496.

(89) Wang, H.; Hsu, A.; Wu, J.; Kong, J.; Palacios, T. Graphene-Based Ambipolar RF Mixers. IEEE Electron Device Letters 2010, 31, 906–908.

(90) Wang, L.; Meric, I.; Huang, P. Y.; Gao, Q.; Gao, Y.; Tran, H.; Taniguchi, T.; Watanabe, K.; Campos, L. M.; Muller, D. A.; et al. One-Dimensional Electrical Contact to a Two-Dimensional Material. Science 2013, 342, 614–617.

(91) Liu, G.; Stillman, W.; Rumyantsev, S.; Shao, Q.; Shur, M.; Balandin, A. A. Low-Frequency Electronic Noise in the Double-Gate Single-Layer Graphene Transistors. Applied Physics Letters 2009, 95, 033103.

(92) Lin, Y.-M.; Dimitrakopoulos, C.; Jenkins, K. A.; Farmer, D. B.; Chiu, H.-Y.; Grill, A.; Avouris, P. 100-GHz Transistors from Wafer-Scale Epitaxial Graphene. Science 2010, 327, 662–662.

(93) Forrest, S. R. The Path to Ubiquitous and Low-Cost Organic Electronic Appliances on Plastic. Nature 2004, 428, 911–918.

(94) Stutzmann, N. Self-Aligned, Vertical-Channel, Polymer Field-Effect Transistors. Science 2003, 299, 1881–1884.

(95) Sirringhaus, H. High-Resolution Inkjet Printing of All-Polymer Transistor Circuits. Science 2000, 290, 2123–2126.

(96) Gu, G.; Kane, M. G.; Doty, J. E.; Firester, A. H. Electron Traps and Hysteresis in Pentacene-Based Organic Thin-Film Transistors. Applied Physics Letters 2005, 87, 243512.

(97) Zilker, S. J.; Detcheverry, C.; Cantatore, E.; de Leeuw, D. M. Bias Stress in Organic Thin-Film Transistors and Logic Gates. Applied Physics Letters 2001, 79, 1124.

(98) Bäcklund, T. G.; Österbacka, R.; Stubb, H.; Bobacka, J.; Ivaska, A. Operating Principle of Polymer Insulator Organic Thin-Film Transistors Exposed to Moisture. Journal of Applied Physics 2005, 98, 074504.

(99) Song, K.; Noh, J.; Jun, T.; Jung, Y.; Kang, H.-Y.; Moon, J. Fully Flexible Solution-Deposited ZnO Thin-Film Transistors. Advanced Materials 2010, 22, 4308–4312.

(100) Sun, Y.; Menard, E.; Rogers, J. A.; Kim, H.-S.; Kim, S.; Chen, G.; Adesida, I.; Dettmer, R.; Cortez, R.; Tewksbury, A. Gigahertz Operation in Flexible Transistors on Plastic Substrates. Applied Physics Letters 2006, 88, 183509.

(101) Pitanti, A.; Vitiello, M. S.; Romeo, L.; Coquillat, D.; Teppe, F.; Knap, W.; Ercolani, D.; Sorba, L.; Tredicucci, A. Semiconductor Nanowire Field-Effect Transistors: Towards High-Frequency THz Detectors. In; Razeghi, M.; Baranov, A. N.; Everitt, H. O.; Zavada, J. M.; Manzur, T., Eds.; 2012; p. 84960N.

(102) Kagan, C. R. Organic-Inorganic Hybrid Materials as Semiconducting Channels in Thin-Film Field-Effect Transistors. Science 1999, 286, 945–947.

(103) Dai, M.-K.; Lian, J.-T.; Lin, T.-Y.; Chen, Y.-F. High-Performance Transparent and Flexible Inorganic Thin Film Transistors: A Facile Integration of Graphene Nanosheets and Amorphous InGaZnO. Journal of Materials Chemistry C 2013, 1, 5064.

(104) Rogers, J. A. Electronic Materials: Making Graphene for Macroelectronics. Nature Nanotechnology 2008, 3, 254–255.

(105) Zhao, X.; Zhang, Q.; Chen, D.; Lu, P. Enhanced Mechanical Properties of Graphene-Based Poly(vinyl Alcohol) Composites. Macromolecules 2010, 43, 2357–2363.

(106) Faccio, R.; Denis, P. A.; Pardo, H.; Goyenola, C.; Mombrú, Á. W. Mechanical Properties of Graphene Nanoribbons. Journal of Physics: Condensed Matter 2009, 21, 285304.

(107) Kim, B. J.; Jang, H.; Lee, S.-K.; Hong, B. H.; Ahn, J.-H.; Cho, J. H. High-Performance Flexible Graphene Field Effect Transistors with Ion Gel Gate Dielectrics. Nano Letters 2010, 10, 3464–3466.

(108) Tian, H.; Yang, Y.; Xie, D.; Cui, Y.-L.; Mi, W.-T.; Zhang, Y.; Ren, T.-L. Wafer-Scale Integration of Graphene-Based Electronic, Optoelectronic and Electroacoustic Devices. Scientific Reports 2014, 4.

(109) El-Kady, M. F.; Strong, V.; Dubin, S.; Kaner, R. B. Laser Scribing of High-Performance and Flexible Graphene-Based Electrochemical Capacitors. Science 2012, 335, 1326–1330.

(110) Geim, A. K.; Grigorieva, I. V. Van Der Waals Heterostructures. Nature 2013, 499, 419–425.

(111) Deepak, F. L.; Mayoral, A.; Steveson, A. J.; Mejía-Rosales, S.; Blom, D. A.; José-Yacamán, M. Insights into the Capping and Structure of $MoS_2$ Nanotubes as Revealed by Aberration-Corrected STEM. Nanoscale 2010, 2, 2286.

(112) Mak, K. F.; Lee, C.; Hone, J.; Shan, J.; Heinz, T. F. Atomically Thin $MoS_2$: A New Direct-Gap Semiconductor. Physical Review Letters 2010, 105.

(113) Lee, Y.-H.; Zhang, X.-Q.; Zhang, W.; Chang, M.-T.; Lin, C.-T.; Chang, K.-D.; Yu, Y.-C.; Wang, J. T.-W.; Chang, C.-S.; Li, L.-J.; et al. Synthesis of Large-Area $MoS_2$ Atomic Layers with Chemical Vapor Deposition. Advanced Materials 2012, 24, 2320–2325.

(114) Kuc, A.; Zibouche, N.; Heine, T. Influence of Quantum Confinement on the Electronic Structure of the Transition Metal Sulfide $TS_2$. Physical Review B 2011, 83.

(115) Wang, Q. H.; Kalantar-Zadeh, K.; Kis, A.; Coleman, J. N.; Strano, M. S. Electronics and Optoelectronics of Two-Dimensional Transition Metal Dichalcogenides. Nature Nanotechnology 2012, 7, 699–712.

(116) Watanabe, K.; Taniguchi, T.; Kanda, H. Direct-Bandgap Properties and Evidence for Ultraviolet Lasing of Hexagonal Boron Nitride Single Crystal. Nature Materials 2004, 3, 404–409.

(117) Dean, C. R.; Young, A. F.; Meric, I.; Lee, C.; Wang, L.; Sorgenfrei, S.; Watanabe, K.; Taniguchi, T.; Kim, P.; Shepard, K. L.; et al. Boron Nitride Substrates for High-Quality Graphene Electronics. Nature Nanotechnology 2010, 5, 722–726.

(118) Bolotin, K. I.; Sikes, K. J.; Jiang, Z.; Klima, M.; Fudenberg, G.; Hone, J.; Kim, P.; Stormer, H. L. Ultrahigh Electron Mobility in Suspended Graphene. Solid State Communications 2008, 146, 351–355.

(119) Farmer, D. B.; Golizadeh-Mojarad, R.; Perebeinos, V.; Lin, Y.-M.; Tulevski, G. S.; Tsang, J. C.; Avouris, P. Chemical Doping and Electron−Hole Conduction Asymmetry in Graphene Devices. Nano Letters 2009, 9, 388–392.

(120) Wei, D.; Liu, Y.; Wang, Y.; Zhang, H.; Huang, L.; Yu, G. Synthesis of N-Doped Graphene by Chemical Vapor Deposition and Its Electrical Properties. Nano Letters 2009, 9, 1752–1758.

(121) Mišković, Z. L.; Sharma, P.; Goodman, F. O. Ionic Screening of Charged Impurities in Electrolytically Gated Graphene. Physical Review B 2012, 86.

(122) Dong, X.; Fu, D.; Fang, W.; Shi, Y.; Chen, P.; Li, L.-J. Doping Single-Layer Graphene with Aromatic Molecules. Small 2009, 5, 1422–1426.

(123) Xia, F.; Perebeinos, V.; Lin, Y.; Wu, Y.; Avouris, P. The Origins and Limits of Metal–graphene Junction Resistance. Nature Nanotechnology 2011, 6, 179–184.

(124) Nagashio, K.; Nishimura, T.; Kita, K.; Toriumi, A. Metal/graphene Contact as a Performance Killer of Ultra-High Mobility Graphene Analysis of Intrinsic Mobility and Contact Resistance. In; IEEE, 2009; pp. 1–4.

(125) Smith, J. T.; Franklin, A. D.; Farmer, D. B.; Dimitrakopoulos, C. D. Reducing Contact Resistance in Graphene Devices through Contact Area Patterning. ACS Nano 2013, 7, 3661–3667.

(126) Giovannetti, G.; Khomyakov, P.; Brocks, G.; Karpan, V.; van den Brink, J.; Kelly, P. Doping Graphene with Metal Contacts. Physical Review Letters 2008, 101.

(127) Gong, C.; Lee, G.; Shan, B.; Vogel, E. M.; Wallace, R. M.; Cho, K. First-Principles Study of Metal–graphene Interfaces. Journal of Applied Physics 2010, 108, 123711.

(128) Léonard, F.; Talin, A. A. Electrical Contacts to One- and Two-Dimensional Nanomaterials. Nature Nanotechnology 2011, 6, 773–783.

(129) Brabec, C. J.; Shaheen, S. E.; Winder, C.; Sariciftci, N. S.; Denk, P. Effect of LiF/metal Electrodes on the Performance of Plastic Solar Cells. Applied Physics Letters 2002, 80, 1288.

(130) Kim, J. Y.; Lee, K.; Coates, N. E.; Moses, D.; Nguyen, T.-Q.; Dante, M.; Heeger, A. J. Efficient Tandem Polymer Solar Cells Fabricated by All-Solution Processing. Science 2007, 317, 222–225.

(131) DiBenedetto, S. A.; Facchetti, A.; Ratner, M. A.; Marks, T. J. Molecular Self-Assembled Monolayers and Multilayers for Organic and Unconventional Inorganic Thin-Film Transistor Applications. Advanced Materials 2009, 21, 1407–1433.

(132) Seo, J. H.; Yang, R.; Brzezinski, J. Z.; Walker, B.; Bazan, G. C.; Nguyen, T.-Q. Electronic Properties at Gold/Conjugated-Polyelectrolyte Interfaces. Advanced Materials 2009, 21, 1006–1011.

(133) Liu, F.; Page, Z. A.; Duzhko, V. V.; Russell, T. P.; Emrick, T. Conjugated Polymeric Zwitterions as Efficient Interlayers in Organic Solar Cells. Advanced Materials 2013, 25, 6868–6873.

(134) Page, Z. A.; Duzhko, V. V.; Emrick, T. Conjugated Thiophene-Containing Polymer Zwitterions: Direct Synthesis and Thin Film Electronic Properties. Macromolecules 2013, 46, 344–351.

(135) Wu, H.; Huang, F.; Mo, Y.; Yang, W.; Wang, D.; Peng, J.; Cao, Y. Efficient Electron Injection from a Bilayer Cathode Consisting of Aluminum and Alcohol-/Water-Soluble Conjugated Polymers. Advanced Materials 2004, 16, 1826–1830.

(136) Li, G.; Chu, C.-W.; Shrotriya, V.; Huang, J.; Yang, Y. Efficient Inverted Polymer Solar Cells. Applied Physics Letters 2006, 88, 253503.

(137) Pacilé, D.; Papagno, M.; Rodríguez, A.; Grioni, M.; Papagno, L.; Girit, ç.; Meyer, J.; Begtrup, G.; Zettl, A. Near-Edge X-Ray Absorption Fine-Structure Investigation of Graphene. Physical Review Letters 2008, 101.

(138) Schultz, B. J.; Patridge, C. J.; Lee, V.; Jaye, C.; Lysaght, P. S.; Smith, C.; Barnett, J.; Fischer, D. A.; Prendergast, D.; Banerjee, S. Imaging Local Electronic Corrugations and Doped Regions in Graphene. Nature Communications 2011, 2, 372.

(139) Song, S. M.; Park, J. K.; Sul, O. J.; Cho, B. J. Determination of Work Function of Graphene under a Metal Electrode and Its Role in Contact Resistance. Nano Letters 2012, 12, 3887–3892.

(140) Hillmyer, M. Block Copolymer Synthesis. Current Opinion in Solid State and Materials Science 1999, 4, 559–564.

(141) Leibler, L. Theory of Microphase Separation in Block Copolymers. Macromolecules 1980, 13, 1602–1617.

(142) Segalman, R. A.; Hexemer, A.; Kramer, E. J. Effects of Lateral Confinement on Order in Spherical Domain Block Copolymer Thin Films. Macromolecules 2003, 36, 6831–6839.

(143) Stoykovich, M. P. Directed Assembly of Block Copolymer Blends into Nonregular Device-Oriented Structures. Science 2005, 308, 1442–1446.

(144) Xiao, S.; Yang, X.; Edwards, E. W.; La, Y.-H.; Nealey, P. F. Graphoepitaxy of Cylinder-Forming Block Copolymers for Use as Templates to Pattern Magnetic Metal Dot Arrays. Nanotechnology 2005, 16, S324–S329.

(145) Ashok, B.; Muthukumar, M.; Russell, T. P. Confined Thin Film Diblock Copolymer in the Presence of an Electric Field. The Journal of Chemical Physics 2001, 115, 1559.

(146) Pereira, G. G.; Williams, D. R. M. Diblock Copolymer Melts in Electric Fields: The Transition from Parallel to Perpendicular Alignment Using a Capacitor Analogy. Macromolecules 1999, 32, 8115–8120.

(147) Morkved, T. L.; Lu, M.; Urbas, A. M.; Ehrichs, E. E.; Jaeger, H. M.; Mansky, P.; Russell, T. P. Local Control of Microdomain Orientation in Diblock Copolymer Thin Films with Electric Fields. Science 1996, 273, 931–933.

(148) Xu, T.; Hawker, C. J.; Russell, T. P. Interfacial Energy Effects on the Electric Field Alignment of Symmetric Diblock Copolymers. Macromolecules 2003, 36, 6178–6182.

(149) Jeong, U.; Ryu, D. Y.; Kho, D. H.; Kim, J. K.; Goldbach, J. T.; Kim, D. H.; Russell, T. P. Enhancement in the Orientation of the Microdomain in Block Copolymer Thin Films upon the Addition of Homopolymer. Advanced Materials 2004, 16, 533–536.

(150) Wong, D. T.; Mullin, S. A.; Battaglia, V. S.; Balsara, N. P. Relationship between Morphology and Conductivity of Block-Copolymer Based Battery Separators. Journal of Membrane Science 2012, 394-395, 175–183.

(151) Kim, S. H.; Misner, M. J.; Xu, T.; Kimura, M.; Russell, T. P. Highly Oriented and Ordered Arrays from Block Copolymers via Solvent Evaporation. Advanced Materials 2004, 16, 226–231.

(152) Lohmueller, T.; Bock, E.; Spatz, J. P. Synthesis of Quasi-Hexagonal Ordered Arrays of Metallic Nanoparticles with Tuneable Particle Size. Advanced Materials 2008, 20, 2297–2302.

(153) Kästle, G.; Boyen, H.-G.; Weigl, F.; Lengl, G.; Herzog, T.; Ziemann, P.; Riethmüller, S.; Mayer, O.; Hartmann, C.; Spatz, J. P.; et al. Micellar Nanoreactors—Preparation and Characterization of Hexagonally Ordered Arrays of Metallic Nanodots. Advanced Functional Materials 2003, 13, 853–861.

(154) Gowrishankar, V.; Miller, N.; McGehee, M. D.; Misner, M. J.; Ryu, D. Y.; Russell, T. P.; Drockenmuller, E.; Hawker, C. J. Fabrication of Densely Packed, Well-Ordered, High-Aspect-Ratio Silicon Nanopillars over Large Areas Using Block Copolymer Lithography. Thin Solid Films 2006, 513, 289–294.

(155) Park, S.; Wang, J.-Y.; Kim, B.; Russell, T. P. From Nanorings to Nanodots by Patterning with Block Copolymers. Nano Letters 2008, 8, 1667–1672.

(156) Zu, X.; Hu, X.; Lyon, L. A.; Deng, Y. In Situ Fabrication of Ordered Nanoring Arrays via the Reconstruction of Patterned Block Copolymer Thin Films. Chemical Communications 2010, 46, 7927.

(157) Park, S.; Yavuzcetin, O.; Kim, B.; Tuominen, M. T.; Russell, T. P. A Simple Top-Down/Bottom-Up Approach to Sectored, Ordered Arrays of Nanoscopic Elements Using Block Copolymers. Small 2009, 5, 1064–1069.

(158) Han, M.; Özyilmaz, B.; Zhang, Y.; Kim, P. Energy Band-Gap Engineering of Graphene Nanoribbons. Physical Review Letters 2007, 98.

(159) Cresti, A.; Nemec, N.; Biel, B.; Niebler, G.; Triozon, F.; Cuniberti, G.; Roche, S. Charge Transport in Disordered Graphene-Based Low Dimensional Materials. Nano Research 2008, 1, 361–394.

(160) Sprinkle, M.; Ruan, M.; Hu, Y.; Hankinson, J.; Rubio-Roy, M.; Zhang, B.; Wu, X.; Berger, C.; de Heer, W. A. Scalable Templated Growth of Graphene Nanoribbons on SiC. Nature Nanotechnology 2010, 5, 727–731.

(161) Kato, T.; Hatakeyama, R. Site- and Alignment-Controlled Growth of Graphene Nanoribbons from Nickel Nanobars. Nature Nanotechnology 2012, 7, 651–656.

(162) Kosynkin, D. V.; Higginbotham, A. L.; Sinitskii, A.; Lomeda, J. R.; Dimiev, A.; Price, B. K.; Tour, J. M. Longitudinal Unzipping of Carbon Nanotubes to Form Graphene Nanoribbons. Nature 2009, 458, 872–876.

(163) Cano-Márquez, A. G.; Rodríguez-Macías, F. J.; Campos-Delgado, J.; Espinosa-González, C. G.; Tristán-López, F.; Ramírez-González, D.; Cullen, D. A.; Smith, D. J.; Terrones, M.; Vega-Cantú, Y. I. Ex-MWNTs: Graphene Sheets and Ribbons Produced by Lithium Intercalation and Exfoliation of Carbon Nanotubes. Nano Letters 2009, 9, 1527–1533.

(164) Jiao, L.; Zhang, L.; Wang, X.; Diankov, G.; Dai, H. Narrow Graphene Nanoribbons from Carbon Nanotubes. Nature 2009, 458, 877–880.

(165) Li, X.; Wang, X.; Zhang, L.; Lee, S.; Dai, H. Chemically Derived, Ultrasmooth Graphene Nanoribbon Semiconductors. Science 2008, 319, 1229–1232.

(166) Wang, X.; Ouyang, Y.; Li, X.; Wang, H.; Guo, J.; Dai, H. Room-Temperature All-Semiconducting Sub-10-nm Graphene Nanoribbon Field-Effect Transistors. Physical Review Letters 2008, 100.

(167) Bai, J.; Zhong, X.; Jiang, S.; Huang, Y.; Duan, X. Graphene Nanomesh. Nature Nanotechnology 2010, 5, 190–194.

(168) Sinitskii, A.; Tour, J. M. Patterning Graphene through the Self-Assembled Templates: Toward Periodic Two-Dimensional Graphene Nanostructures with Semiconductor Properties. Journal of the American Chemical Society 2010, 132, 14730–14732.

(169) Liang, X.; Jung, Y.-S.; Wu, S.; Ismach, A.; Olynick, D. L.; Cabrini, S.; Bokor, J. Formation of Bandgap and Subbands in Graphene Nanomeshes with Sub-10 nm Ribbon Width Fabricated via Nanoimprint Lithography. Nano Letters 2010, 10, 2454–2460.

(170) Zeng, Z.; Huang, X.; Yin, Z.; Li, H.; Chen, Y.; Li, H.; Zhang, Q.; Ma, J.; Boey, F.; Zhang, H. Fabrication of Graphene Nanomesh by Using an Anodic Aluminum Oxide Membrane as a Template. Advanced Materials 2012, 24, 4138–4142.

(171) Park, S.; Wang, J.-Y.; Kim, B.; Chen, W.; Russell, T. P. Solvent-Induced Transition from Micelles in Solution to Cylindrical Microdomains in Diblock Copolymer Thin Films. Macromolecules 2007, 40, 9059–9063.

(172) Xu, T.; Stevens, J.; Villa, J. A.; Goldbach, J. T.; Guarini, K. W.; Black, C. T.; Hawker, C. J.; Russell, T. P. Block Copolymer Surface Reconstruction: A Reversible Route to Nanoporous Films. Advanced Functional Materials 2003, 13, 698–702.

(173) Rafiee, J.; Mi, X.; Gullapalli, H.; Thomas, A. V.; Yavari, F.; Shi, Y.; Ajayan, P. M.; Koratkar, N. A. Wetting Transparency of Graphene. Nature Materials 2012, 11, 217–222.

(174) Wang, S.; Zhang, Y.; Abidi, N.; Cabrales, L. Wettability and Surface Free Energy of Graphene Films. Langmuir 2009, 25, 11078–11081.

(175) Ryu, D. Y. A Generalized Approach to the Modification of Solid Surfaces. Science 2005, 308, 236–239.

(176) Zhao, H.; Gu, W.; Sterner, E.; Russell, T. P.; Coughlin, E. B.; Theato, P. Highly Ordered Nanoporous Thin Films from Photocleavable Block Copolymers. Macromolecules 2011, 44, 6433–6440.

(177) Gu, X.; Dorsey, P.; Russell, T. P. High Density and Large Area Arrays of Silicon Oxide Pillars with Tunable Domain Size for Mask Etch Applications. Advanced Materials 2012, 24, 5505–5511.

(178) Gu, X.; Liu, Z.; Gunkel, I.; Chourou, S. T.; Hong, S. W.; Olynick, D. L.; Russell, T. P. High Aspect Ratio Sub-15 nm Silicon Trenches From Block Copolymer Templates. Advanced Materials 2012, 24, 5688–5694.

(179) Ferrari, A. C.; Meyer, J. C.; Scardaci, V.; Casiraghi, C.; Lazzeri, M.; Mauri, F.; Piscanec, S.; Jiang, D.; Novoselov, K. S.; Roth, S.; et al. Raman Spectrum of Graphene and Graphene Layers. Physical Review Letters 2006, 97.

(180) Kim, M.; Safron, N. S.; Han, E.; Arnold, M. S.; Gopalan, P. Fabrication and Characterization of Large-Area, Semiconducting Nanoperforated Graphene Materials. Nano Letters 2010, 10, 1125–1131.

(181) Pedersen, T.; Flindt, C.; Pedersen, J.; Mortensen, N.; Jauho, A.-P.; Pedersen, K. Graphene Antidot Lattices: Designed Defects and Spin Qubits. Physical Review Letters 2008, 100.

(182) Ryu, S.; Maultzsch, J.; Han, M. Y.; Kim, P.; Brus, L. E. Raman Spectroscopy of Lithographically Patterned Graphene Nanoribbons. ACS Nano 2011, 5, 4123–4130.

(183) Gupta, A.; Chen, G.; Joshi, P.; Tadigadapa, S.; Eklund. Raman Scattering from High-Frequency Phonons in Supported n-Graphene Layer Films. Nano Letters 2006, 6, 2667–2673.

(184) Das, A.; Pisana, S.; Chakraborty, B.; Piscanec, S.; Saha, S. K.; Waghmare, U. V.; Novoselov, K. S.; Krishnamurthy, H. R.; Geim, A. K.; Ferrari, A. C.; et al. Monitoring Dopants by Raman Scattering in an Electrochemically Top-Gated Graphene Transistor. Nature Nanotechnology 2008, 3, 210–215.

(185) Wang, M.; Fu, L.; Gan, L.; Zhang, C.; Rümmeli, M.; Bachmatiuk, A.; Huang, K.; Fang, Y.; Liu, Z. CVD Growth of Large Area Smooth-Edged Graphene Nanomesh by Nanosphere Lithography. Scientific Reports 2013, 3.

(186) Shi, Z.; Yang, R.; Zhang, L.; Wang, Y.; Liu, D.; Shi, D.; Wang, E.; Zhang, G. Patterning Graphene with Zigzag Edges by Self-Aligned Anisotropic Etching. Advanced Materials 2011, 23, 3061–3065.

(187) Geng, D.; Wu, B.; Guo, Y.; Luo, B.; Xue, Y.; Chen, J.; Yu, G.; Liu, Y. Fractal Etching of Graphene. Journal of the American Chemical Society 2013, 135, 6431–6434.

(188) Campos, L. C.; Manfrinato, V. R.; Sanchez-Yamagishi, J. D.; Kong, J.; Jarillo-Herrero, P. Anisotropic Etching and Nanoribbon Formation in Single-Layer Graphene. Nano Letters 2009, 9, 2600–2604.

(189) Liu, J.; Cai, H.; Yu, X.; Zhang, K.; Li, X.; Li, J.; Pan, N.; Shi, Q.; Luo, Y.; Wang, X. Fabrication of Graphene Nanomesh and Improved Chemical Enhancement for Raman Spectroscopy. The Journal of Physical Chemistry C 2012, 116, 15741–15746.

(190) Yang, R.; Shi, Z.; Zhang, L.; Shi, D.; Zhang, G. Observation of Raman G-Peak Split for Graphene Nanoribbons with Hydrogen-Terminated Zigzag Edges. Nano Letters 2011, 11, 4083–4088.

(191) Guo, H.; Lu, N.; Wang, L.; Wu, X.; Zeng, X. C. Tuning Electronic and Magnetic Properties of Early Transition-Metal Dichalcogenides via Tensile Strain. The Journal of Physical Chemistry C 2014, 118, 7242–7249.

(192) Ionescu, R.; Wang, W.; Chai, Y.; Mutlu, Z.; Ruiz, I.; Favors, Z.; Wickramaratne, D.; Neupane, M.; Zavala, L.; Lake, R.; et al. Synthesis of Atomically Thin MoS2 Triangles and Hexagrams and Their Electrical Transport Properties. IEEE Transactions on Nanotechnology 2014, 13, 749–754.

(193) Ge, W.; Kawahara, K.; Tsuji, M.; Ago, H. Large-Scale Synthesis of $NbS_2$ Nanosheets with Controlled Orientation on Graphene by Ambient Pressure CVD. Nanoscale 2013, 5, 5773.

(194) Kim, S.; Konar, A.; Hwang, W.-S.; Lee, J. H.; Lee, J.; Yang, J.; Jung, C.; Kim, H.; Yoo, J.-B.; Choi, J.-Y.; et al. High-Mobility and Low-Power Thin-Film Transistors Based on Multilayer $MoS_2$ Crystals. Nature Communications 2012, 3, 1011.

(195) Radisavljevic, B.; Radenovic, A.; Brivio, J.; Giacometti, V.; Kis, A. Single-Layer $MoS_2$ Transistors. Nature Nanotechnology 2011, 6, 147–150.

(196) Yoon, Y.; Ganapathi, K.; Salahuddin, S. How Good Can Monolayer $MoS_2$ Transistors Be? Nano Letters 2011, 11, 3768–3773.

(197) Brivio, J.; Alexander, D. T. L.; Kis, A. Ripples and Layers in Ultrathin $MoS_2$ Membranes. Nano Letters 2011, 11, 5148–5153.

(198) Coleman, J. N.; Lotya, M.; O'Neill, A.; Bergin, S. D.; King, P. J.; Khan, U.; Young, K.; Gaucher, A.; De, S.; Smith, R. J.; et al. Two-Dimensional Nanosheets Produced by Liquid Exfoliation of Layered Materials. Science 2011, 331, 568–571.

(199) Zeng, Z.; Yin, Z.; Huang, X.; Li, H.; He, Q.; Lu, G.; Boey, F.; Zhang, H. Single-Layer Semiconducting Nanosheets: High-Yield Preparation and Device Fabrication. Angewandte Chemie International Edition 2011, 50, 11093–11097.

(200) Najmaei, S.; Liu, Z.; Zhou, W.; Zou, X.; Shi, G.; Lei, S.; Yakobson, B. I.; Idrobo, J.-C.; Ajayan, P. M.; Lou, J. Vapour Phase Growth and Grain Boundary Structure of Molybdenum Disulphide Atomic Layers. Nature Materials 2013, 12, 754–759.

(201) Van der Zande, A. M.; Huang, P. Y.; Chenet, D. A.; Berkelbach, T. C.; You, Y.; Lee, G.-H.; Heinz, T. F.; Reichman, D. R.; Muller, D. A.; Hone, J. C. Grains and Grain Boundaries in Highly Crystalline Monolayer Molybdenum Disulphide. Nature Materials 2013, 12, 554–561.

(202) Balendhran, S.; Ou, J. Z.; Bhaskaran, M.; Sriram, S.; Ippolito, S.; Vasic, Z.; Kats, E.; Bhargava, S.; Zhuiykov, S.; Kalantar-zadeh, K. Atomically Thin Layers of $MoS_2$ via a Two Step Thermal Evaporation–exfoliation Method. Nanoscale 2012, 4, 461.

(203) Lin, Y.-C.; Zhang, W.; Huang, J.-K.; Liu, K.-K.; Lee, Y.-H.; Liang, C.-T.; Chu, C.-W.; Li, L.-J. Wafer-Scale $MoS_2$ Thin Layers Prepared by MoO3 Sulfurization. Nanoscale 2012, 4, 6637.

(204) Liu, K.-K.; Zhang, W.; Lee, Y.-H.; Lin, Y.-C.; Chang, M.-T.; Su, C.-Y.; Chang, C.-S.; Li, H.; Shi, Y.; Zhang, H.; et al. Growth of Large-Area and Highly Crystalline $MoS_2$ Thin Layers on Insulating Substrates. Nano Letters 2012, 12, 1538–1544.

(205) Putz, J.; Aegerter, M. A. $MoS_x$ Thin Films by Thermolysis of a Single-Source Precursor. Journal of Sol-Gel Science and Technology 2000, 19, 821–824.

(206) Putz, J.; Aegerter, M. A. Liquid Film Deposition of Chalcogenide Thin Films. Journal of Sol-Gel Science and Technology 2003, 26, 807–811.

(207) Wang, H.; Yu, L.; Lee, Y.-H.; Shi, Y.; Hsu, A.; Chin, M. L.; Li, L.-J.; Dubey, M.; Kong, J.; Palacios, T. Integrated Circuits Based on Bilayer $MoS_2$ Transistors. Nano Letters 2012, 12, 4674–4680.

(208) Wu, R. J.; Odlyzko, M. L.; Mkhoyan, K. A. Determining the Thickness of Atomically Thin $MoS_2$ and $WS_2$ in the TEM. Ultramicroscopy 2014, 147, 8–20.

(209) Tan, L. K.; Liu, B.; Teng, J. H.; Guo, S.; Low, H. Y.; Loh, K. P. Atomic Layer Deposition of a $MoS_2$ Film. Nanoscale 2014, 6, 10584.

(210) Li, B.; Yang, S.; Huo, N.; Li, Y.; Yang, J.; Li, R.; Fan, C.; Lu, F. Growth of Large Area Few-Layer or Monolayer $MoS_2$ from Controllable $MoO_3$ Nanowire Nuclei. RSC Advances 2014, 4, 26407.

(211) Li, H.; Zhang, Q.; Yap, C. C. R.; Tay, B. K.; Edwin, T. H. T.; Olivier, A.; Baillargeat, D. From Bulk to Monolayer $MoS_2$: Evolution of Raman Scattering. Advanced Functional Materials 2012, 22, 1385–1390.

(212) Lee, C.; Yan, H.; Brus, L. E.; Heinz, T. F.; Hone, J.; Ryu, S. Anomalous Lattice Vibrations of Single- and Few-Layer $MoS_2$. ACS Nano 2010, 4, 2695–2700.

(213) Splendiani, A.; Sun, L.; Zhang, Y.; Li, T.; Kim, J.; Chim, C.-Y.; Galli, G.; Wang, F. Emerging Photoluminescence in Monolayer $MoS_2$. Nano Letters 2010, 10, 1271–1275.

(214) Mouri, S.; Miyauchi, Y.; Matsuda, K. Tunable Photoluminescence of Monolayer $MoS_2$ via Chemical Doping. Nano Letters 2013, 13, 5944–5948.

(215) Coehoorn, R.; Haas, C.; Dijkstra, J.; Flipse, C.; de Groot, R.; Wold, A. Electronic Structure of $MoSe_2$, $MoS_2$, and $WSe_2$. I. Band-Structure Calculations and Photoelectron Spectroscopy. Physical Review B 1987, 35, 6195–6202.

(216) Zhan, Y.; Liu, Z.; Najmaei, S.; Ajayan, P. M.; Lou, J. Large-Area Vapor-Phase Growth and Characterization of $MoS_2$ Atomic Layers on a $SiO_2$ Substrate. Small 2012, 8, 966–971.

(217) Song, J.-G.; Park, J.; Lee, W.; Choi, T.; Jung, H.; Lee, C. W.; Hwang, S.-H.; Myoung, J. M.; Jung, J.-H.; Kim, S.-H.; et al. Layer-Controlled, Wafer-Scale, and Conformal Synthesis of Tungsten Disulfide Nanosheets Using Atomic Layer Deposition. ACS Nano 2013, 7, 11333–11340.

(218) Zhao, W.; Ghorannevis, Z.; Chu, L.; Toh, M.; Kloc, C.; Tan, P.-H.; Eda, G. Evolution of Electronic Structure in Atomically Thin Sheets of $WS_2$ and $WSe_2$. ACS Nano 2013, 7, 791–797.

(219) Berkdemir, A.; Gutiérrez, H. R.; Botello-Méndez, A. R.; Perea-López, N.; Elías, A. L.; Chia, C.-I.; Wang, B.; Crespi, V. H.; López-Urías, F.; Charlier, J.-C.; et al. Identification of Individual and Few Layers of $WS_2$ Using Raman Spectroscopy. Scientific Reports 2013, 3.

(220) Kośmider, K.; Fernández-Rossier, J. Electronic Properties of the $MoS_2$-$WS_2$ Heterojunction. Physical Review B 2013, 87.

(221) Anto Jeffery, A.; Nethravathi, C.; Rajamathi, M. Two-Dimensional Nanosheets and Layered Hybrids of $MoS_2$ and $WS_2$ through Exfoliation of Ammoniated $MS_2$ (M = Mo,W). The Journal of Physical Chemistry C 2014, 118, 1386–1396.

(222) Mann, J.; Ma, Q.; Odenthal, P. M.; Isarraraz, M.; Le, D.; Preciado, E.; Barroso, D.; Yamaguchi, K.; von Son Palacio, G.; Nguyen, A.; et al. 2-Dimensional Transition Metal Dichalcogenides with Tunable Direct Band Gaps: $MoS_{2(1-X)}Se_{2x}$ Monolayers. Advanced Materials 2014, 26, 1399–1404.